

12

THE VIEWS AND CONCLUSIONS CONTAINED IN THIS DOCUMENT ARE THOSE OF THE AUTHOR AND SHOULD NOT BE INTERPRETED AS NECESSARILY REPRESENTING THE OFFICIAL POLICIES, EITHER EXPRESSED OR IMPLIED, OF THE ADVANCED RESEARCH PROJECTS AGENCY OF THE U.S. GOVERNMENT

AD A 047684

ONE METER KrF LASER SYSTEM

J.C. Hsia, J.H. Jacob, J.A. Mangano and M. Rokni
Avco Everett Research Laboratory, Inc.
2385 Revere Beach Parkway
Everett MA 02149

Semi-Annual Report for Period 23 August 1976 to 22 February 1977

APPROVED FOR PUBLIC RELEASE; DISTRIBUTION UNLIMITED.

Sponsored by
DEFENSE ADVANCED RESEARCH PROJECTS AGENCY
DARPA Order No. 3125

DDC
RECEIVED
DEC 19 1977
E

Monitored by
OFFICE OF NAVAL RESEARCH
DEPARTMENT OF THE NAVY
Arlington VA 22217

AD NO. 1
DDC FILE COPY

FOREWORD

DARPA Order No.: 3125

Program Code No.:

Contractor: Avco Everett Research Laboratory, Inc.

Effective Date of Contract: August 23, 1976

Contract Expiration Date: November 23, 1977

Contract No.: N00014-76-C-1032

Short Title of Work: One Meter KrF Laser System

Principal Investigator and Phone No.: J.A. Mangano,
(617) 389-3000, Ext. 725

Scientific Officer: Director Physics Program, Physical Sciences Div.
Office of Naval Research
800 North Quincy Street
Arlington, VA 22217

Amount of Contract: \$568,758

UNCLASSIFIED

SECURITY CLASSIFICATION OF THIS PAGE (When Data Entered)

REPORT DOCUMENTATION PAGE		READ INSTRUCTIONS BEFORE COMPLETING FORM
1. REPORT NUMBER	2. GOVT ACCESSION NO.	3. RECIPIENT'S CATALOG NUMBER
4. TITLE (and Subtitle)		5. TYPE OF REPORT & PERIOD COVERED
One Meter KrF Laser System.		Semi-Annual Report, 23 Aug 76 - 22 Feb 77
6. AUTHOR(s)		6. PERFORMING ORG. REPORT NUMBER
J. C. Hsia, J. H. Jacob, J. A. Mangano M. Rokni		8. CONTRACT OR GRANT NUMBER
9. PERFORMING ORGANIZATION NAME AND ADDRESS		10. PROGRAM ELEMENT, PROJECT, TASK AREA & WORK UNIT NUMBERS
Avco Everett Research Laboratory, Inc. 2385 Revere Beach Parkway Everett, Massachusetts 02149		
11. CONTROLLING OFFICE NAME AND ADDRESS		12. REPORT DATE
Defense Advanced Research Projects Agency DARPA Order No. 1806		11 22 Feb 77
14. MONITORING AGENCY NAME & ADDRESS (if different from Controlling Office)		13. NUMBER OF PAGES
Office of Naval Research Department of the Navy Arlington, Virginia 22217		97
15. SECURITY CLASS. (of this report)		15. DECLASSIFICATION DOWNGRADING SCHEDULE
Unclassified		12 93 P.
16. DISTRIBUTION STATEMENT (of this Report)		
Approved for public release; distribution unlimited.		
17. DISTRIBUTION STATEMENT (of the abstract entered in Block 20, if different from Report)		
Approved for public release; distribution unlimited.		
18. SUPPLEMENTARY NOTES		
15 N00014-76-C-1032, V DARPA Order 1806		
19. KEY WORDS (Continue on reverse side if necessary and identify by block number)		
Excimer Lasers	Electron Beam Excitation	Laser Medium Gain and Absorption
Rare Gas-Monohalide Lasers	High Power Lasers	Laser Energy Extraction
KrF Lasers	Laser Kinetics	Excited State Formation and Quenching
XeF Lasers	Magnetically Guided E-Beams	
ABSTRACT (Continue on reverse side if necessary and identify by block number)		
<p>This interim report covers research directed towards electron beam and electron beam sustained discharge pumping of rare gas-halide lasers. The key issues being addressed are: (1) upper laser level formation and quenching, (2) laser medium gain and absorption, (3) laser energy extraction, (4) kinetic modeling, (5) attainable laser efficiency and energy scaling, and (6) spatial uniformity in excitation. Using a magnetically guided E-beam to pump a KrF laser, 0.2 joules of laser output was obtained in an active laser volume of 8.5 liter, with 9% intrinsic laser efficiency. Laser performance</p>		

DD FORM 1473
1 JAN 73

EDITION OF 1 NOV 65 IS OBSOLETE

UNCLASSIFIED

SECURITY CLASSIFICATION OF THIS PAGE (When Data Entered)

UNCLASSIFIED

SECURITY CLASSIFICATION OF THIS PAGE(When Data Entered)

agree with predictions of the kinetic model over the range of operating conditions investigated.

UNCLASSIFIED

SECURITY CLASSIFICATION OF THIS PAGE(When Data Entered)

REPORT SUMMARY

SEARCHED	<input checked="" type="checkbox"/>
SERIALIZED	<input type="checkbox"/>
INDEXED	<input type="checkbox"/>
FILED	<input type="checkbox"/>
JAN 1978	
FBI - NEW YORK	
A	

A. PROGRAM APPROACH AND SCOPE

DARPA/ONR-sponsored research at AERL on rare gas-monohalide laser systems has shown the new class of lasers to have the potential for both high efficiency and high average power. In particular, preliminary calculations indicated that with direct electron beam pumping, carefully designed high average power KrF^* lasers can have an overall system efficiency as high as 10%. With e-beam controlled discharge pumping of this laser, overall efficiencies as high as 12% are possible. The objectives of the present program are to confirm these predictions and assess the applicability of the rare gas-monohalide lasers for DARPA missions.

In order to carry out this research in an expeditious and efficient manner, various parts of the underlying physics are resolved on a small scale (20 cm) device. These experiments provide the various parameter values (cross sections, rate constants, etc.) necessary to develop comprehensive laser models which predict laser performance and scaling. In addition, large scale KrF^* laser experiments are performed on a one-meter device to confirm the predictive capability of the laser models.

B. ACCOMPLISHMENTS AND FINDINGS

This interim report covers the period 23 August 1976 to 22 February 1977. The major results obtained in this reporting period are summarized as follows:

- (1) Important KrF^* formation and quenching rates have been measured.
- (2) The use of these rates in a kinetics model enabled us to predict KrF^* laser performance.
- (3) Construction and testing of the 1-meter e-beam/e-beam sustained laser device were completed.
- (4) Large scale e-beam energy deposition nonuniformities were measured and their causes identified.
- (5) Magnetic beam confinement was proposed and implemented.
- (6) The effectiveness of e-beam confinement was demonstrated both experimentally and theoretically.
- (7) A laser output energy of 102 joules with an active laser volume of 8.5 liters (12 J/l) at an intrinsic laser efficiency of 9% was obtained.
- (8) The laser results confirmed the validity of our model calculations.

C. PLANS FOR NEXT PERIOD

For the next period, work on the one-meter device will explore e-beam sustained discharge pumping of KrF^* . Discharge pumping is attractive for two reasons: first, it offers the possibility of higher laser efficiency because the upper laser level is pumped through rare gas metastable channels and second, for repped operation, foil heating is much less severe since only a small fraction of the pump power needs to be applied through a foil. Theoretical and small scale experimental studies at AERL have shown that under suitable conditions, stable discharges can be made in rare gas halide laser mixtures at excitation levels necessary for efficient laser action. The

study showed that a KrF^* intrinsic laser efficiency of 15% at a discharge enhancement ratio of 4 (discharge energy into laser mixture/e-beam energy in) should be possible.

In the next period we will also study the XeF^* laser, both using pure e-beam excitation and e-beam sustained discharge pumping. Although XeF^* lasers have not yet been demonstrated to be as efficient as KrF^* , our kinetics, gain, and absorption studies show that XeF^* possess many of the same characteristics of KrF^* (i.e., high gain, efficient upper level formation, low self-absorption), so it holds the promise of high efficiency. An efficient XeF^* laser has the advantage that at 350 nm the laser output lies in a wavelength region where atmospheric absorption and scattering are low, so there is no need for wavelength conversion in order to meet DARPA requirements.

**BLANK PAGES
IN THIS
DOCUMENT
WERE NOT
FILMED**

TABLE OF CONTENTS

<u>Section</u>	<u>Page</u>
Report Summary	1
List of Illustrations	7
I. INTRODUCTION	9
II. SMALL SCALE EXPERIMENTS	11
A. KrF [*] Formation and Quenching Rate Measurements	11
B. KrF [*] Laser Medium Gain and Absorption Experiments	22
C. Summary of Major Results	31
III. ENERGY EXTRACTION AND SCALING	33
IV. ONE-METER E-BEAM/E-BEAM SUSTAINED DISCHARGE DEVICE	41
V. E-BEAM MEASUREMENTS AND INITIAL KrF [*] LASING EXPERIMENTS	51
VI. E-BEAM CONFINEMENT BY EXTERNALLY APPLIED GUIDE FIELD	65
VII. E-BEAM PUMPED KrF [*] LASER EXPERIMENTS	79
REFERENCES	85
 <u>Appendices</u>	
A FAST BEAM CURRENT DENSITY FLUCTUATION	87
B HIGH ENERGY ELECTRON SCATTERING	93

LIST OF ILLUSTRATIONS

<u>Figure</u>		<u>Page</u>
1	KrF* Fluorescence Intensity vs Pressure and Kr Concentration	13
2	Spontaneous Emission from E-Beam Excited Mixtures of Kr/F ₂ /Ar at Various Total Pressures	15
3	KrF* Fluorescence Efficiency	17
4	Schematic of the Apparatus Used to Measure KrF* Gain and Loss	23
5	Oscillograms Showing the Probe and Reference Photodiode Signal at Various Stages of a Gain Measurement	25
6	Gain and Loss Measurements as a Function of Wavelength Near the KrF* ($2\Sigma_{1/2} \rightarrow 2\Sigma_{1/2}$) Emission Band	27
7	Laser Power Extraction Efficiency at Optimum Output Coupling Plotted against g_0L with αL as a Variable Parameter	36
8	Laser Output Flux Normalized to the Saturation Flux Plotted as a Function of g_0L with αL as a Variable Parameter	37
9	Optimum Output Coupling as a Function of g_0L and αL	38
10	Cold Cathode E-Gun	42
11	Photograph of the Cathode and E-Gun Chamber	43
12	Marx Generator Circuit	45
13	One Meter KrF Laser Cavity	46
14	One Meter KrF Laser Discharge Circuitry	48
15	Photograph of Entire Device	49
16	E-Gun Cathode Voltage and Current Characteristic	52
17	E-Beam Energy Deposition Measurement Apparatus	54

<u>Figure</u>		<u>Page</u>
18	The Beam Collectors in the Faraday Cup Array are Constructed from Graphite to Minimize Albedo	55
19	Transverse Beam Profiles for Gun Anode-Cathode Spacings of 6 and 8 cm	56
20	Vertical Fluorescence Intensity Scans at Various Distances from the Foil	58
21	Vertical Fluorescence Intensity Seen with Various E-Gun Anode-Cathode Spacings	59
22	Beam Current Density Variations in the Maxwell E-Gun	60
23	KrF ⁺ Laser Burn Pattern (No Magnetic Field)	63
24	The Larmor Radius of a Beam Electron at the Gun Anode is Plotted Against the Product of Beam Current Density and Beam Height	66
25	Calculated Contours of Constant E-Beam Energy Deposition without External Magnetic Field	68
26	Calculated Contours of Constant E-Beam Energy Deposition with 800 Gauss Externally Applied Magnetic Field	70
27	Magnetic Field Coil	71
28	Cross Sections of E-Gun and Laser Cavity with Magnetic Field Coils	73
29	Horizontal Magnetic Field Measured Along Centerline of Device	74
30	Comparison of Transmitted E-Beam Current with and without Externally Applied Magnetic Field	75
31	Magnetic Steering of the E-Beam (1 mil Titanium Foil)	77
32	Laser Output Burn Pattern	80
33	E-Beam and Laser Characteristics	81
A-1	Potentials for Both Unipolar and Bipolar Diodes as Shown	89
A-2	Equipotential Contours for the Case of Local Anode Ion Sources	90
A-3	E-Gun Cathode Voltage and Current with SS and Tungsten Anode Screens	92

1. INTRODUCTION

The objective of the present program is to determine whether the rare gas-monohalide (KrF^* at 248 nm and XeF^* at 350 nm) can be used to make efficient, high power lasers. Preliminary calculations indicated that with direct e-beam pumping, carefully designed high average power KrF^* lasers can have an overall system efficiency as high as 10%. With e-beam controlled discharge pumping of this laser, overall system efficiencies as high as 12% are possible.

In order to confirm these predictions, comprehensive computer models for both KrF^* and XeF^* are developed to reliably predict the performance of large scale versions of these lasers. These models describe the important and underlying physics which include:

- E-beam Energy Deposition
 - Spatial and Temporal Uniformity
- E-beam Energy Partitioning
 - Ionization and Excitation
- KrF^* Formation Kinetics
 - Ion Channel Formation
 - Metastable Channel Formation
 - Discharge Physics
- KrF^* Laser Power Extraction
 - KrF^* Quenching Kinetics
 - Gain and Absorption
 - Lower and Upper State Kinetics

In order to assess the applicability of the rare gas monohalide lasers for DARPA missions in an expeditious and efficient manner, various parts of the underlying physics are resolved on a small scale (20 cm) device. These experiments provide the various parameter values (cross sections, rate constants, etc.) necessary to develop comprehensive laser models. In addition, large scale KrF^* laser experiments are performed on a one-meter device to confirm the predictive capability of the laser models. Single pulse energy density and intrinsic laser efficiency (laser output energy/energy deposited) with direct e-beam pumping are measured over a range of operating conditions.

In the first section of this report the results of the small scale experiments are described. In these experiments the kinetic rates, gain and absorption coefficients in the KrF^* system were measured. The important predictions of the kinetic model code using the results of these measurements will be summarized. Then we will describe the design and construction of the one-meter e-beam/e-beam sustained discharge device. The results of the initial device characterization experiments are reported and, finally, the results of e-beam pumped KrF^* laser experiments carried out on this device will be presented.

II. SMALL SCALE EXPERIMENTS

Three conditions must be met in order for a laser to have a chance of being efficient. First, the channeling of energy from the external pump to the upper laser level must be efficient. Second, once formed, the upper states must be stimulated at a rate much faster than the rate of spontaneous radiative decay and collisional quenching. Third, the laser medium absorption at the laser wavelength must be small so that a high laser cavity flux can be maintained for effective stimulated emission without high absorption losses. During this reporting period the small scale (20 cm) e-beam device has been used to understand the KrF^* formation kinetics, measure the ratio of three-body collisional quenching, and measure the gain and excited species absorption in typical KrF^* laser mixtures.

A. KrF^* FORMATION AND QUENCHING RATE MEASUREMENTS

The 20-cm E-gun device, capable of delivering a beam with an energy of 150 kV and a current density of $0.16 - 5 \text{ A/cm}^2$ for 300 nsec has been described previously.⁽¹⁾ The cross-sectional dimensions of the electron beam were 2 cm x 22 cm. The beam deposited its energy in typical KrF^* mixtures which were contained in a teflon cell. The cell was 0.5 cm in the beam direction to insure uniform energy deposition over the volume of the cell up to pressures of 4 atmospheres.⁽²⁾

⁽¹⁾ Mangano, J.A., and Jacob, J.H., Appl. Phys. Lett. 27, 495 (1975)

⁽²⁾ Jacob, J.H., J. Appl. Phys. 45, 467 (1974).

The KrF^* fluorescence amplitude was measured using a pair of apertures to define the solid angle of the detected radiation from the e-beam excited mixtures. A calibrated photodiode was used to detect the emission. A 5 nm bandpass filter centered at 250 nm was placed in front of the photodiode. The KrF^* fluorescence amplitude in watts/cm^3 could then be related to the flux seen at the photodiode by integrating over the distributed fluorescence source excited by the e-beam. Isotropic KrF^* fluorescence was assumed in this calculation. This condition was assured by utilizing a small beam current density ($\leq 5 \text{ A/cm}^2$) to avoid the effects of amplified spontaneous emission. Because KrF is unbound in the ground state the medium is optically thin.

The KrF^* steady state fluorescence intensity for mixtures containing 1% and 15% Kr is shown in Figure 1 as a function of total mixture pressure. Similar data were also taken with mixtures containing 3% and 6% Kr. Although the KrF^* fluorescence amplitude peaks at a pressure of 1.0 - 2.5 atmospheres, the KrF^* laser output (under comparable experimental conditions) from these mixtures can continue to rise with increasing pressure up to approximately 4 atm.⁽³⁾ In a laser device, the concentration of KrF^* can be reduced by a suitably high laser cavity flux which can compete with and perhaps dominate all other quenching processes. These results imply that the decrease in KrF^* fluorescence amplitude for high pressures is caused by quenching of the KrF^* directly and is not a process which interferes with the formation of KrF^* . Because the cavity dimension in the direction of the e-beam is only 0.5 cm the energy deposited in the mixture increases linearly

⁽³⁾ Brau, C.A., and Ewing, J.J. private communication.

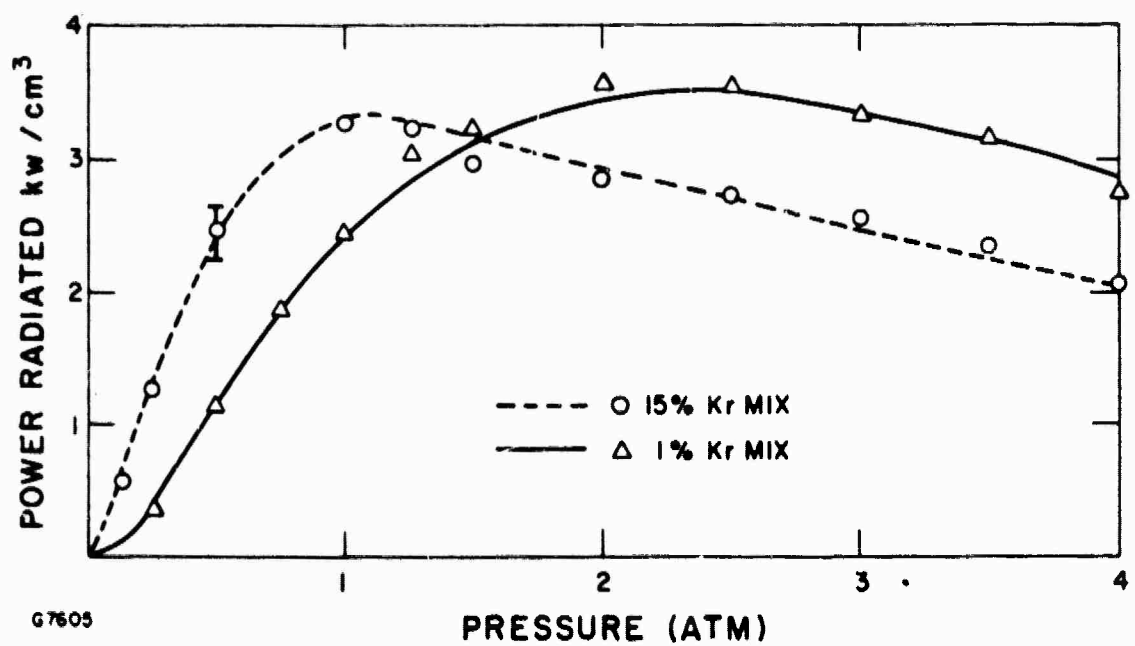
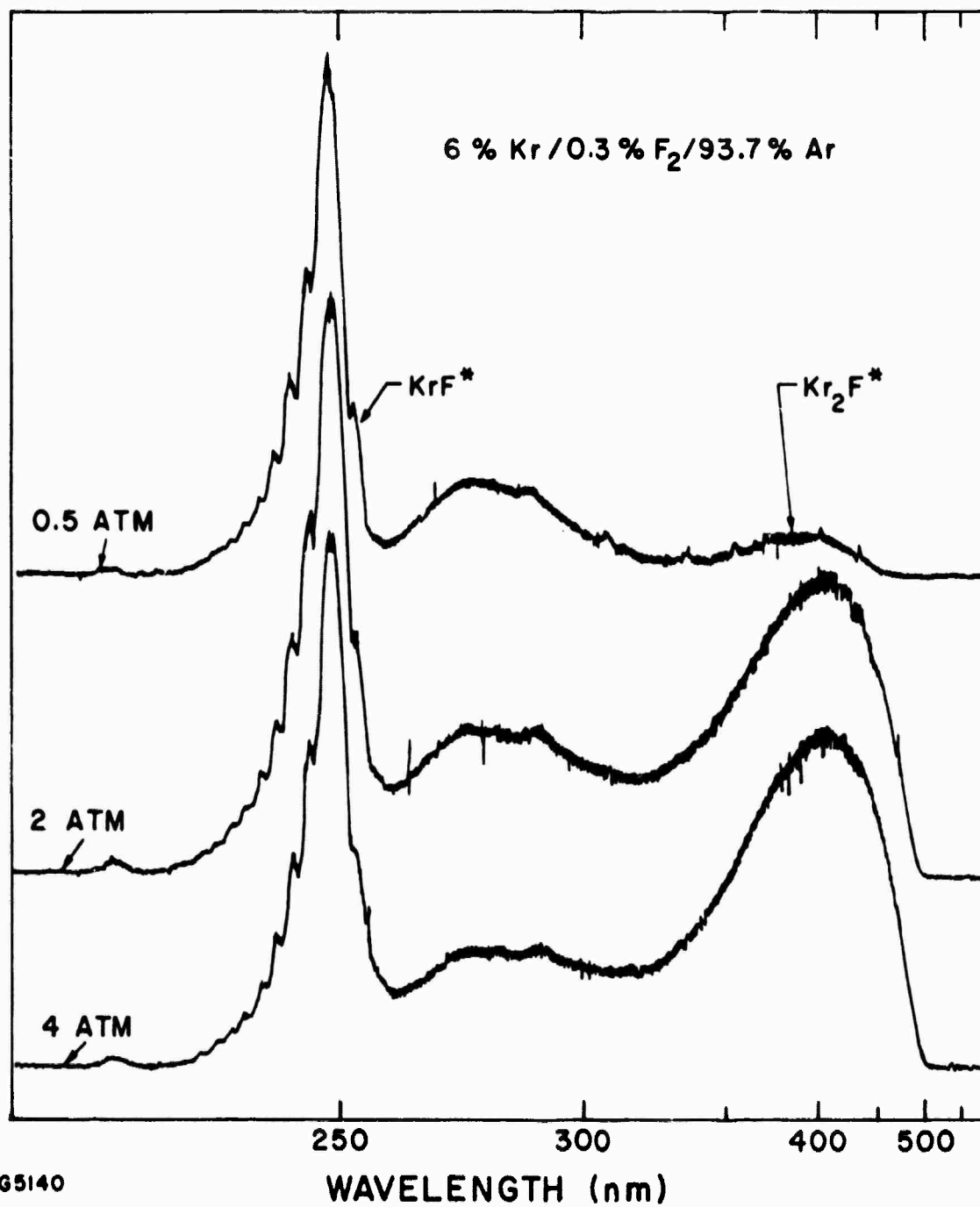


Figure 1 KrF^* Fluorescence Intensity vs Pressure and Kr Concentration

with pressure. As a result, if there is no KrF^* quenching the fluorescence will rise linearly with pressure. At high pressures a two body quenching will result in a constant radiation at high pressure. For three body quenching processes the KrF^* fluorescence amplitude eventually decreases at high pressures. Consequently, a second important conclusion is that for the mixtures considered here, three body quenching processes eventually dominate at high pressure.

In order to obtain further information concerning the KrF^* quenching processes, spectra shown in Figure 2 of the spontaneous emission from e-beam excited mixtures were obtained at mixture pressures of 0.5, 2 and 4 atmospheres. The uncalibrated spectral intensity scale is approximately logarithmic. At 0.5 atmosphere essentially all of the radiation from the mixture is contained in the $\text{KrF}^* \ ^2\Sigma_{1/2} \rightarrow \ ^2\Sigma_{1/2}$ band at 248 nm. However, two other broad bands, containing much less energy, are observable. The first is centered at 415 nm and has been identified with the $\ ^2B_2 \rightarrow A_1$ transition of the excited triatomic Kr_2F^* .⁽⁴⁾ The other broad band, centered roughly at 270 - 280 nm, is most likely a combination of radiation from the $\ ^2\Sigma - \ ^2\Pi$ band of KrF^* and perhaps radiation from the excited triatomics Ar_2F^* ⁽⁴⁾ and ArKrF^* . Identification of the Kr_2F^* and Ar_2F^* bands was inferred by observing the radiation from binary mixtures of Ar/F_2 and Kr/F_2 . From the Kr/F_2 mix we observed the same spectra except that some of the structure in the band centered at 270-280 nm disappeared. From the Ar/F_2 mixture, the spectra showed only a very broad band centered at 290-300 nm which has been identified as Ar_2F^* radiation. The spectrum obtained at a

⁽⁴⁾ Krauss, M. NBS, private communication



G5140

Figure 2 Spontaneous Emission from E-Beam Excited Mixtures of Kr/F₂/Ar at Various Total Pressures

total mixture pressure of 4 atm indicates that, compared with the 0.5 atm spectrum, essentially the same energy is contained in the $\text{KrF}^* 2\Sigma_{1/2} \rightarrow 2\Sigma_{1/2}$ band, although the e-beam energy deposited increased by a factor of ~ 8 . This spectrum indicates that most of the additional energy deposited by the e-beam was channeled to Kr_2F^* . Consequently, (because of the laser result of Reference 3 and our measurements which will be discussed subsequently), three body KrF^* quenching mechanisms ultimately result in Kr_2F^* formation.

In order to determine the KrF^* fluorescence efficiency from the data shown in Figure 1, the beam energy density deposited in the mixture was determined by monitoring the pressure rise in the cavity. The steady state power deposited in the mixture was then calculated. These measurements agreed with beam energy deposition calculations for these mixtures to within 10%.⁽²⁾ The KrF^* fluorescence efficiency (shown in Figure 3) was then computed as a function of total mixture pressure by dividing the fluorescence amplitudes (shown in Figure 1) by the corresponding beam power density deposited.

Since the mixture contains $\geq 85\%$ argon, the high energy beam electrons deposit most of their energy into the argon. Approximately 55% of this energy goes into forming argon ions,⁽⁵⁾ Ar^+ . At low pressures (< 1 atm), these ions rapidly recombine with the negative ions F^- with a diffusion-limited equivalent two body rate constant of approximately $2-3 \times 10^{-6} \text{ cm}^3/\text{sec}$ ⁽⁶⁾ to form ArF^* . The ArF^* can radiate at 193 nm and form

(5) Peterson, L.R. and Allen, J.E., J. Chem. Phys. 56, 6068 (1972).

(6) Flannery, in Case Studies in Atomic Collision Physics 2, edited by McDaniel, E.W., and McDowell, M.R.C., North Holland, Amsterdam, 1972, p. 3

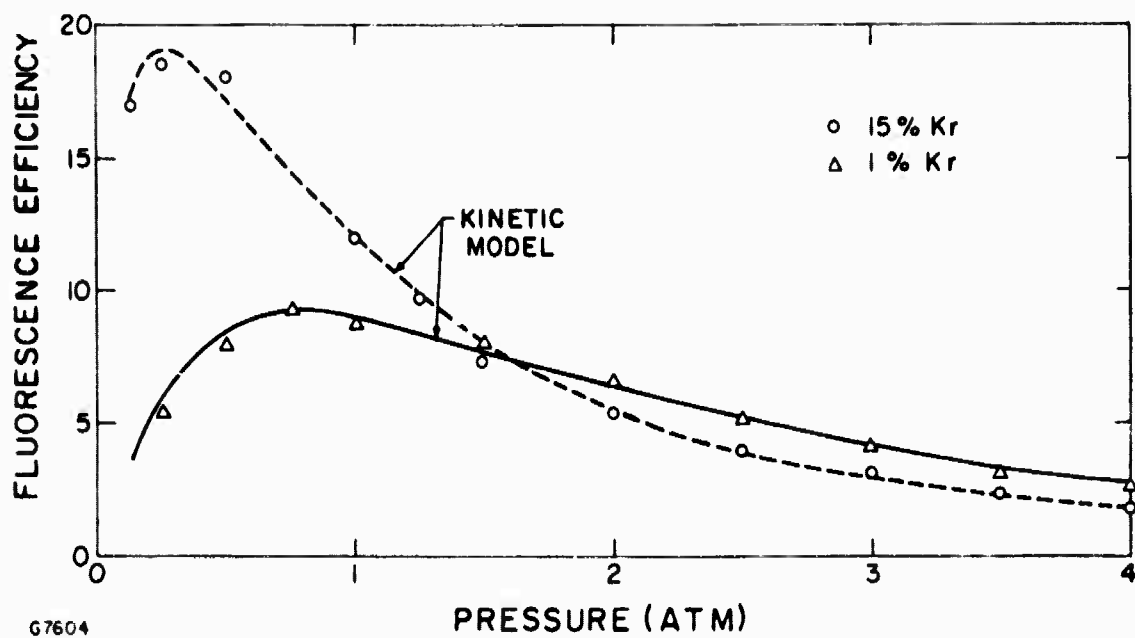


Figure 3 KrF Fluorescence Efficiency

ground state Ar and F atoms. The radiative lifetime of ArF^* has been calculated to be 10 nsec.⁽⁷⁾ However, at sufficiently high krypton number densities, the krypton will exchange with the ArF^* to form KrF^* .⁽⁸⁾ In fact, the decrease in the KrF^* fluorescence efficiency seen in Figure 3 at low total mixture pressures can be explained if some significant number of the ArF^* radiate before the exchange reaction can occur.

At high pressure the argon ions and neutrals form Ar_2^+ with a three-body rate constant of $2.5 \times 10^{-31} \text{ cm}^6/\text{sec}$.⁽⁹⁾ The Ar_2^+ can undergo charge transfer with Kr to form Kr^+ with a rate constant of $7.5 \times 10^{-10} \text{ cm}^3/\text{sec}$.⁽¹⁰⁾ For lean krypton mixes the Kr^+ will combine with the negative fluorine ions to form KrF^* . As the Kr density is increased, Kr_2^+ will be formed. We have verified that by varying the e-beam pump power by a factor of 30, Kr_2^+ recombines with F^- to form KrF^* .⁽¹¹⁾ The KrF^* can spontaneously decay with a lifetime of 6.5 nsec (calculated by Dunning and Hay)⁽¹²⁾ or can be collisionally quenched. Three body quenching of KrF^* is primarily responsible for the decrease in the KrF^* fluorescence efficiency seen at higher pressures. From Figure 3 this collisional quenching is seen to be dependent on the krypton density. The dependency on krypton partial pressure can

(7) Michels, H., United Technologies, private communication.

(8) Ewing, J.J., LLL, private communication.

(9) McDaniel, E.W., Cermak, V., Dalgarno, A., Ferguson, E.E., and Friedman, L., Ion-Molecule Reactions (Wiley-Interscience, New York, (1970) p. 338.

(10) Bohme, K.K., Adams, N.G., Moselman, M., Dunkin, D.B., and Ferguson, E.E., J. Chem. Phys. 52, 5094 (1970).

(11) For a detailed discussion of this verification procedure see Rokni, M., Jacob, J.H., Mangano, J.A., and Brochu, R., to appear in Appl. Phys. Lett., May (1977).

(12) Dunning, T.H. and Hay, P.J., Appl. Phys. Lett. 28, 649 (1976).

be explained by krypton quenching of KrF^* .⁽¹²⁾ The dominant KrF^* quenching consistent with all the data above are two body quenching by F_2 ⁽¹³⁾



three body quenching by Ar



and three body quenching by Kr



We postulate that ArKrF^* is formed by reaction (2) and is rapidly displaced to form Kr_2F^* . In reaction (3) Kr_2F^* can be formed directly. The excited triatomic Kr_2F^* then radiates (${}^2\text{B}_2 \rightarrow \text{A}_1$) to give a broad band centered at 415 nm. The products $(k_2\tau_1)$ and $(k_3\tau_1)$ of the rate constants (for the KrF^* quenching) and the radiative lifetime τ_1 , can be determined by fitting the predictions of the kinetic model to the KrF^* fluorescence efficiency data. At high pressures (> 1 atm) the resulting fit is especially sensitive to the value assumed for these products. Using the measured value of $(k_1\tau_1) = 5 \times 10^{-18} \text{ cm}^3$ (Ref. 20) and analyzing all the data we have determined the products $(k_2\tau_1)$ and $(k_3\tau_1)$. For mixes containing 1% Kr the effect of reaction (3) on the quenching of KrF^* is $\leq 10\%$. So, from the very lean Kr mixes, a value of $(k_2\tau_1)$ is measured to be

$$k_2\tau_1 = 5.2 \pm 0.5 \times 10^{-40} \text{ cm}^6$$

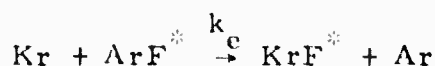
As the Kr partial pressure is increased reaction (3) becomes more important and analyzing the data for the various mixes, the $(k_3\tau_1)$ product is determined to be

$$(k_3\tau_1) = 4.2 \pm 1 \times 10^{-39} \text{ cm}^6$$

(13) Rokni, M., Jacob, J.H. and Mangano, J.A., (unpublished).

Assuming the Dunning and Hay⁽¹²⁾ calculated KrF^* lifetime of 6.5 nsec, $k_2 = 8 \times 10^{-32} \text{ cm}^6/\text{sec}$ and $k_3 = 6.5 \times 10^{-31} \text{ cm}^6/\text{sec}$.

At low pressures (< 0.5 atm), the KrF^* fluorescence efficiency is sensitive to the product of the rate constant, k_e , for the exchange reaction



and the ArF^* radiative lifetime τ_2 . The value for this product giving the best fit to the low pressure data is⁽¹⁴⁾

$$k_e \tau_2 = 5.5 \pm 0.7 \times 10^{-18} \text{ cm}^3$$

Assuming the value of the ArF^* radiative lifetime calculated by Michels,⁽⁷⁾ 10 nsec, the exchange rate constant, k_e , is $5.5 \times 10^{-10} \text{ cm}^3/\text{sec}$.⁽¹⁴⁾ Combination of the exchange reaction and the three body quenching results in the following approximate expression for the steady state⁽¹⁵⁾ fluorescence efficiency η

$$\eta \approx \eta_M \left[\frac{k_e \tau_2 N_{\text{Kr}}}{1 + k_e \tau_2 N_{\text{Kr}}} \right] \left[\frac{1}{1 + k_1 \tau_1 N_{\text{F}_2} + k_2 \tau_1 N_{\text{Ar}}^2 + k_3 \tau_1 N_{\text{Kr}} N_{\text{Ar}}} \right] \quad (4)$$

where N_{Kr} is the density of krypton, N_{F_2} is the density of F_2 and N_{Ar} is the argon density. The code agrees with Eq. (4), over the parameter range investigated in this article, to within 10%. The maximum efficiency η_M for producing KrF^* is about 25%. The curves shown in Figure 3 are a plot of Eq. (4). In Figure 1 the curves plotted are the product of η and the e-beam power deposited.

(14) We have recently measured the exchange reaction by observing the decrease in the ArF^* fluorescence and obtained a value of $k_e \approx 6.5 \times 10^{-18} \text{ cm}^3/\text{sec}$. This work was reported by us at the 7th Winter Colloquium on High Power Visible Lasers, Park City, Utah, Feb. 16-18, (1977).

(15) The steady state assumption is valid because the dominant rates are much less than the 300 ns e-beam pulse.

The saturation flux can now be calculated for the KrF^* laser. If the KrF^* quenching process is included, the saturation flux can be written as

$$\phi_{\text{SAT}} = \frac{h\nu}{\sigma_s \tau_1} (1 + k_1 \tau_1 N_{\text{F}_2} + k_2 \tau_1 N^2 + k_3 \tau_1 N_{\text{Kr}} N) \quad (5)$$

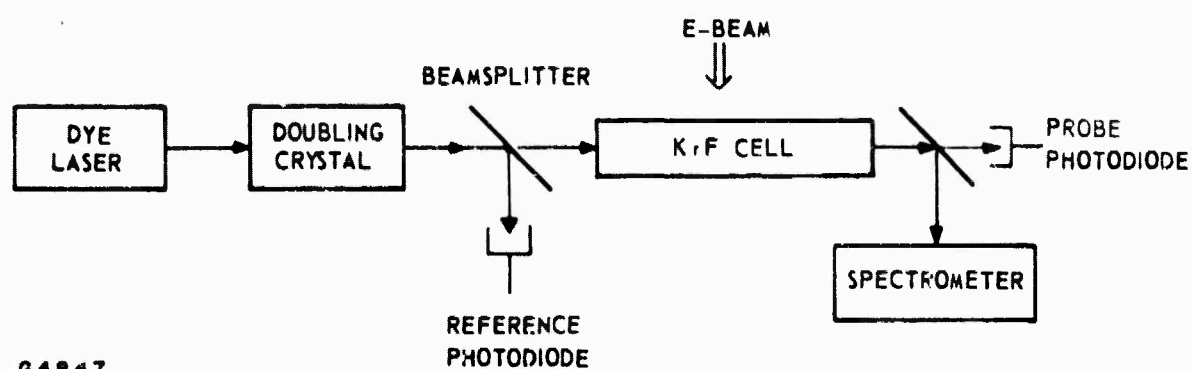
where $h\nu = \text{KrF}^*$ photon energy (5 eV) and $\sigma_s =$ stimulated emission cross section. The product of the KrF^* stimulated emission cross section and life-time have been measured to be $1.6 \times 10^{-24} \text{ cm}^2 \cdot \text{sec}$.⁽¹⁶⁾ This result is in good agreement with that inferred by Tellinghuisen et al.⁽¹⁷⁾ by analyzing the KrF^* fluorescence spectrum. Using the measured value of $\sigma_s \tau_1$ and (5), the saturation flux for the KrF^* laser is approximately 0.85 MW/cm^2 for a mixture containing 0.3% F_2 and 1% Kr at a total pressure of one atmosphere.

(16) Hawryluk, A., Mangano, J.A. and Jacob, J.H., Proceedings of the Third Summer Colloquium on Electronic Transition Lasers, Snowmass, 1976 (unpublished).

(17) Tellinghuisen, J., Hays, A.K., Hoffman, J.M. and Tiscione, G.C., J. Chem. Phys. 65, 4473 (1975).

B. KrF⁺ LASER MEDIUM GAIN AND ABSORPTION EXPERIMENTS

A frequency-doubled, flashlamp-pumped dye laser was built to measure the gain or absorption of a typical e-beam excited KrF⁺ laser mixture (0.3% F₂/6% Kr/93.7% Ar) in the 20 cm device. A schematic diagram of the experimental apparatus is shown in Figure 4. A 12-cm long coaxial flashlamp was used to pump a slowly flowing dye located in a 8 mm inside diameter quartz tube centered in the flashlamp bore. With various mixtures of Coumarin 480 and 522 dyes diluted in methanol, ~10 to 50 mJ/pulse could be produced in the visible wavelength range between 490 and 540 nm, with a linewidth of ~1 Å (FWHM). Two dyes were needed because neither dye alone lased over a sufficiently wide wavelength range. It was found that a mixture of the two dyes lased more efficiently from 490 nm to 510 nm than either dye alone in any part of this region. The dye laser was tuned with a standard grating (1200 lines/mm blazed 17° 27'). The laser pulse duration was ~300 nsec FWHM. The tuned output of the dye laser was focused into a Lithium Formate Monohydrate crystal (LFM) purchased from Lasermetrics, Inc. The conversion efficiency from visible to UV varied between 0.1 and 0.5% over the wavelength band probed. The output of the doubling crystal (170 nsec FWHM) was collimated with a negative lens and filtered to remove the visible fundamental component. The frequency-doubled probe signal was then passed through a UV beam splitter which sampled a few percent of the signal and directed it into a reference photodiode as shown in Figure 4. The remainder of the doubled signal was passed through the excitation cell and collected on the probe photodiode. Part of the signal was reflected and sent into a 0.5 meter Hilger spectrometer so that the wavelength of the doubled dye laser could be determined to within ± 0.2 nm.



64847

Figure 4 Schematic of the Apparatus Used to Measure KrF* Gain and Loss

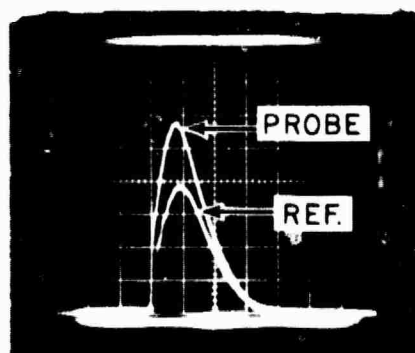
The discharge cavity was constructed of Lucite and stainless steel and capable of withstanding mixture pressures up to 4 atm. In the experiments, beam intensities of 1.5 and 6 A/cm² were used to pre-ionize high-pressure mixtures containing Ar, Kr and F₂. Energy deposition by the e-beam into the lasing mixture was monitored by a Validyne pressure transducer. By measuring the pressure rise from the calibrated transducer, it is possible to calculate the total energy deposited by the e-beam. This is done by calculating the instantaneous temperature rise in the lasing volume from the average pressure rise in the entire cavity. Once this is calculated, and taking into account the fact that ~25% of the e-beam energy is radiated, it is a simple matter to calculate the e-beam energy deposition.

The doubled dye laser was first tuned to 2485 Å and used to probe the evacuated cell. Typical oscillographs of the signals seen by the probe and reference photodiodes are shown in Figure 5. This first shot was used to calibrate the effects of geometry on the reference and photodiode signals. The cell was then filled with 3 atm of the laser mixture (0.3% F₂/6% Kr/93.7% Ar). The probe laser was fired again and the resulting oscillograms are also shown in Figure 5. The decrease in the normalized (to the reference signal) probe signal is attributed to photoabsorption by the F₂ at 2485 Å. The photoabsorption cross section for F₂ which was measured in this manner agreed with the results of Steunenberg and Vogel⁽¹⁸⁾ to within ± 5%. Finally the doubled dye laser was synchronized with the e-beam (1.5 A/cm², 150 kV) and the excited KrF* laser mixture was probed at 2485 Å, the wavelength of the peak gain of the larger KrF* laser band.

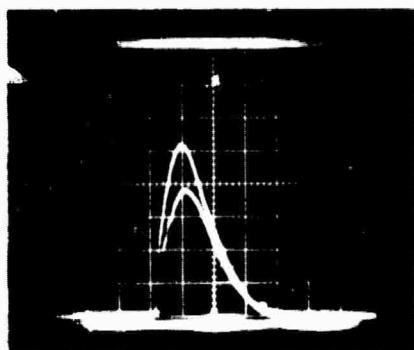
(18) Steunenberg, R. and Vogel, R., J. Am. Chem. Soc. 78, 901 (1956).

GAIN MEASUREMENT
(E-BEAM PUMPING)
 $\lambda = 2485 \text{ \AA}$

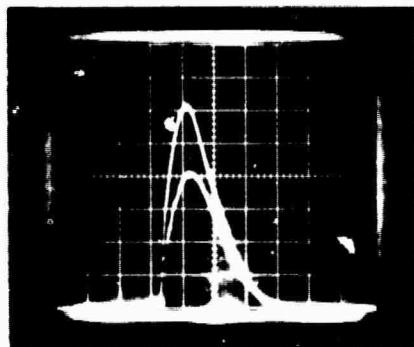
6% K₂/0.3% F₂/93.7% Ar (3 ATM)



CALIBRATION
(CELL EVACUATED)



F₂ ABSORPTION



GAIN, FLUORESCENCE, AND
EXCITED STATE + F₂ ABSORPTION

G5177



TIME (100 ns/DIV)

Figure 5 Oscilloscopes Showing the Probe and Reference Photodiode Signal at Various Stages of a Gain Measurement

Gain at this wavelength was seen as evidenced by an increased normalized probe photodiode signal as shown in Figure 5. KrF^* fluorescence accounts for 0.25 full divisions on the probe signal under e-beam excitation. The doubled dye laser was tuned to a number of wavelengths in the region of the KrF^* ($^2\Sigma_{1/2} \rightarrow ^2\Sigma_{1/2}$) spontaneous emission band. This spontaneous emission band and the narrowing of this band upon lasing are shown at the top of Figure 6. The small signal gain or loss seen at various probe wavelengths were also plotted in this figure. The F_2 photoabsorption has been subtracted from these data. At wavelengths to the red of the KrF^* emission band (≈ 2550 to 2670 \AA) a relatively constant absorption is seen. This nearly constant absorption is being attributed to several ionic and excited species which are listed in Table 1. Table 1 also gives the number densities of these species as predicted by our kinetic code for a 1.5 A/cm^2 and 6 A/cm^2 e-beam current density. Mandl⁽¹⁹⁾ has measured the F^- photo-detachment cross section to be essentially constant at wavelengths between 245 and 270 nm. The photoionization cross sections of Ar^{**} and Kr^{**} have been calculated by H. Hyman.⁽²⁰⁾ Stevens, Gardner and Karo⁽²¹⁾ have recently calculated the Ar_2^+ photoexcitation cross section and determined that it has a peak value of $5 \times 10^{-17} \text{ cm}^2$ at 3000 \AA . The Kr_2^+ photoabsorption cross section was estimated by red shifting the Stevens, Gardner, and Karo Ar_2^+ cross section by 200 \AA .⁽¹³⁾ Finally we have followed M. Krauss's suggestion⁽²²⁾ and assumed that Kr_2F^* will have the same photoexcitation cross section.

(19) Mandl, A., Phys. Rev. A 3, 251 (1971).

(20) Hyman, H., (AERL) private communication.

(21) Stevens, W., Gardner, M. and Karo, A., (unpublished).

(22) Krauss, M., private communication.

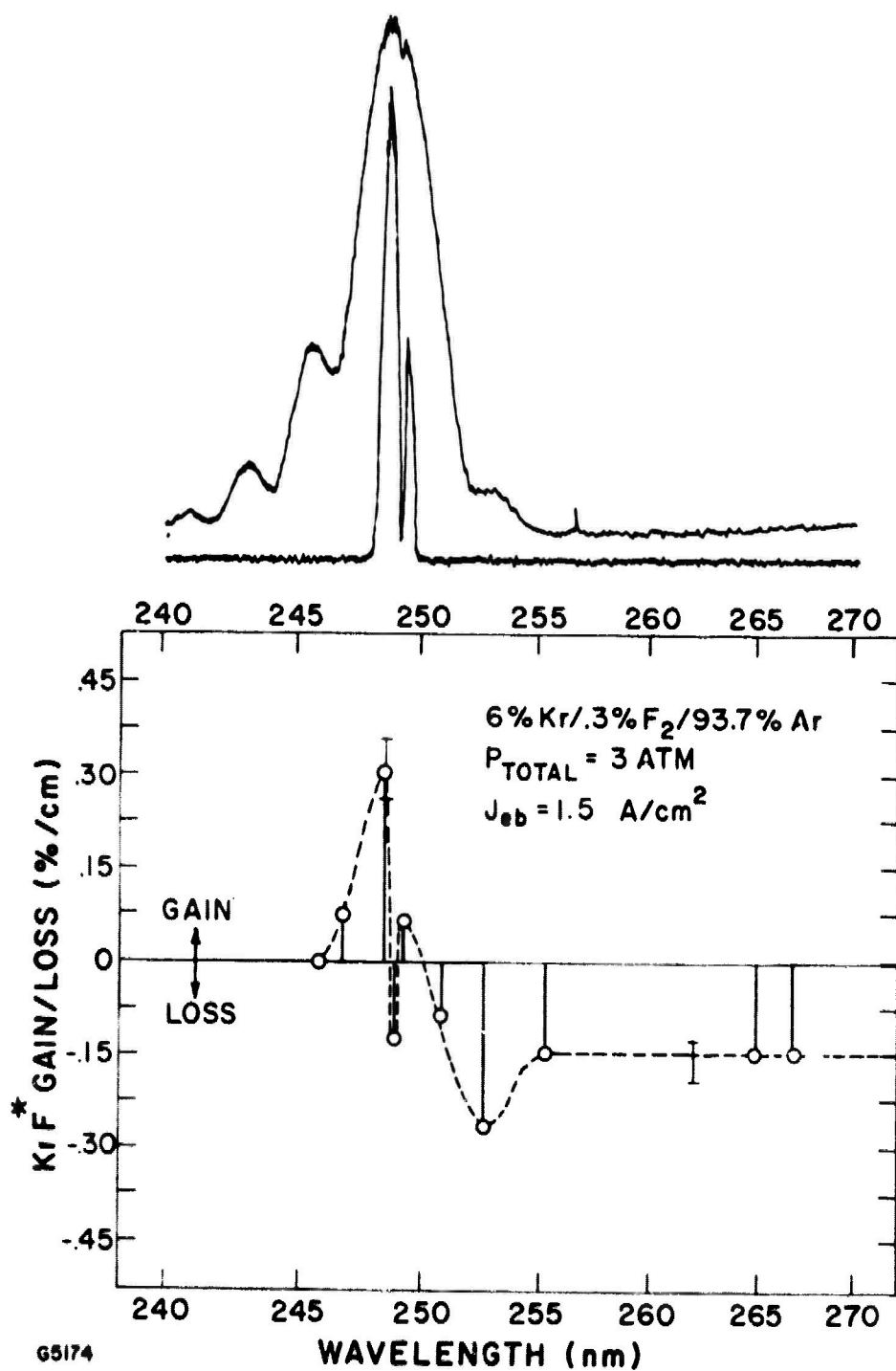


Figure 6 Gain and Loss Measurements as a Function of Wavelength Near the KrF^{*} ($^2\Sigma_{1/2} \rightarrow ^2\Sigma_{1/2}$) Emission Band

The total absorption measured at an e-beam current density of 1.5 A/cm^2 is $1.5 \times 10^{-3} \text{ cm}^{-1}$. From the data listed in Table 1 we calculate an absorption of $1.4 \times 10^{-3} \text{ cm}^{-1}$. At 6 A/cm^2 the measured and calculated values are 4.4×10^{-3} and $4.1 \times 10^{-3} \text{ cm}^{-1}$.

At shorter wavelengths, approximately 2525 \AA , the absorption increases slightly. This increase may be caused by KrF^* self-absorption from the $^2\Sigma_{1/2}$ state to higher-lying Rydberg levels. Indeed the probe laser photon energy (wavelength) at which this additional absorption appears is close to the energy difference between the lowest vibrational levels of the excited $^2\Sigma_{1/2}$ state and the lowest-lying Rydberg level calculated by Dunning and Hay.⁽¹²⁾ At still shorter wavelengths, gain begins to overtake the absorption. At a probe laser wavelength tuned to the center of the small laser peak, gain has become larger than the ionic and excited state absorption. At a slightly shorter wavelength (in the valley between the spectral peaks in the laser output), absorption is again measured. Finally at a probe laser wavelength corresponding to the center of the larger laser band, maximum gain is seen. The effective stimulated emission cross section at this wavelength can be determined by subtracting out the effect of the excited state and ionic absorption (which is assumed constant over this band) from the observed net gain. The effective stimulated emission cross section is defined here as the difference between the actual stimulated emission cross section of the transition and the self-absorption cross section to the higher-lying Rydberg levels. If the kinetic model for the formation and quenching of $\text{KrF}^* (^2\Sigma_{1/2})$ is used to predict the KrF^* number density under the condition of this experiment, the product of the effective stimulated emission cross

TABLE I
KrF* PHOTOABSORPTION

SPECIE	PHOTOABSORPTION CROSS SECTION cm^2	SOURCE	NUMBER DENSITY cm^{-3}		ABSORPTION cm^{-1}	
			1.5 A/cm ²	6 A/cm ²	1.5 A/cm ²	6 A/cm ²
F ⁻	5.6×10^{-18}	MANDL	1.1×10^{14}	2.2×10^{14}	6.2×10^{-4}	1.2×10^{-3}
Kr ₂ ⁺	1.6×10^{-18}	ESTIMATED	4.3×10^{13}	4.9×10^{13}	6.9×10^{-5}	7.9×10^{-5}
Kr ₂ F ⁺	1.6×10^{-18}	ESTIMATED	3.7×10^{14}	1.5×10^{15}	5.9×10^{-4}	2.4×10^{-3}
Ar ₂ ⁺	1.3×10^{-17}	STEVENS ET AL	5.3×10^{12}	1.8×10^{13}	6.9×10^{-5}	2.3×10^{-4}
Ar ⁺⁺ , Kr ⁺⁺	6×10^{-18}	HYMAN	6.2×10^{12}	2.6×10^{13}	3.7×10^{-5}	1.6×10^{-4}
TOTAL CALCULATED ABSORPTION					1.4×10^{-3}	4.1×10^{-3}
TOTAL MEASURED ABSORPTION					1.5×10^{-3}	4.4×10^{-3}

G8167-1

section and the transition lifetime can be determined. This product at peak gain was found to be

$$\sigma_{\text{STIM}} \tau_1 = 1.75 \pm .25 \times 10^{-24} \text{ cm}^2 \text{ - sec}$$

Assuming the Dunning and Hay calculated value⁽¹²⁾ for the KrF^* lifetime of 6.5 nsec, the effective stimulated emission cross section is $2.7 \pm .4 \text{ Å}^2$.

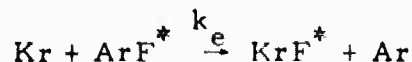
Tellinghuisen, et al.⁽¹⁷⁾ have analyzed the KrF^* spontaneous emission spectrum and found a value of $1.7 \pm .2 \times 10^{-24} \text{ cm}^2 \text{ - sec}$ for the product of the true stimulated emission cross section and lifetime. The agreement between the effective stimulated emission cross section and the actual cross section indicates that the self-absorption losses in the KrF^* laser are small.

Initial measurements taken at an e-beam current density of 5 A/cm^2 show both larger gain and absorption levels for a fixed discharge cell. The measurements taken under this condition indicates a slightly smaller stimulated emission cross section, specifically, $2.4 \pm 0.2 \text{ Å}^2$, again assuming the Dunning and Hay lifetime for KrF^* . This result also agrees favorably with the Tellinghuisen et al. calculated value mentioned earlier. At 5 A/cm^2 , the value we measure is $1.55 \pm .15 \times 10^{-24} \text{ cm}^2 \text{ - sec}$.

C. SUMMARY OF MAJOR RESULTS

The major results obtained this period can be summarized as follows:

- (1) The product of the rate constant, k_e , for the displacement reaction



and the radiative lifetime τ_2 of ArF^* is measured to be

$$k_e \tau_2 = 5.5 \pm 0.7 \times 10^{-18} \text{ cm}^3$$

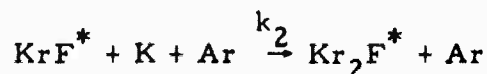
Taking a calculated τ_2 of 10 ns we have

$$k_e = 5.5 \times 10^{-10} \text{ cm}^3/\text{sec}$$

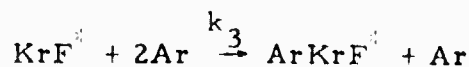
For pressures $\lesssim 1$ atm and for mixtures with sufficient Kr, this reaction effectively competes with the spontaneous decay of ArF^* , making the effective branching ratio from e-beam ionization of Ar to KrF^* essentially unity.

(2) The decrease in KrF^* fluorescence efficiency at high pressures (> 1 atm) is due predominantly to two body collisional quenching of KrF^* by F_2 and three body collisional quenching by Ar and Kr. The decrease is not caused by processes that interfere with the formation of KrF^* . In fact, with sufficient Kr the channeling of energy from e-beam ionization to KrF^* proceeds with essentially unit branching for pressures up to 4 atm. Consequently, by using a sufficiently high laser cavity flux to stimulate KrF^* quickly, the effect of these loss processes can be made negligible.

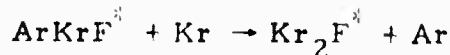
(3) Three body quenching of KrF^* leads to the formation of Kr_2F^* through the reactions



and



followed by



The rate constants k_2 and k_3 are measured to be

$$k_2 = 8 \times 10^{-32} \text{ cm}^6/\text{sec}$$

$$k_3 = 6.5 \times 10^{-31} \text{ cm}^6/\text{sec}$$

if a radiative lifetime of 6.5 nsec is assumed for KrF^* .

(4) The inclusion of these rates into a kinetic model correctly predicts the variation of KrF^* fluorescence with pressure up to 4 atm (highest measured) for all the mixtures tried.

(5) The product of the KrF^* stimulated emission cross section, σ_s , and radiative lifetime, τ_1 , is measured to be $1.6 \times 10^{-24} \text{ cm}^2\text{-sec}$ which agrees with that inferred by Tellinghuisen et al. ⁽¹⁷⁾ Furthermore, the self-absorption of KrF^* at the laser wavelength is small.

(6) The measured excited species absorption at the laser wavelength agrees with those calculated using excited state densities predicted by our model, and using measured or calculated cross sections. The predicted variation of the absorption with different e-beam excitation levels also agree with those measured.

(7) These measured rates and cross sections enable us to calculate the laser saturation flux given by

$$\phi_{\text{sat}} = \frac{h\nu}{\sigma_s \tau_1} (1 + k_1 \tau_1 N_{\text{F}_2} + k_2 \tau_1 N^2 + k_3 \tau_1 N_{\text{Kr}} N)$$

At 1 atm with a typical laser mix of 0.2% F_2 , 5% Kr, balance Ar, we get

$$\phi_{\text{sat}} = 0.8 \text{ MW/cm}^2$$

III. ENERGY EXTRACTION AND SCALING

With the understanding of the dominant formation and quenching processes, one can predict, for a given laser mixture and excitation, KrF^* formation efficiency, gain and excited species absorption. To be able to predict laser efficiency and scaling, one must then look at the interaction of the laser medium with the photon field.

For a KrF^* laser, the lower laser level is repulsive so the lower state lifetime is expected to be very short. In this case the gain can be written as

$$g = g_0 \frac{1}{1 + \phi/\phi_{\text{sat}}}$$

where g_0 is the small signal gain and ϕ is the laser cavity flux. If the laser medium absorption coefficient α times the length, L , of the gain medium is such that $\alpha L \ll 1$ then the optimum extraction efficiency η (laser photons out per upper state formed) is given by

$$\eta \cong \left(1 - \sqrt{\frac{\alpha}{g_0}}\right)^2$$

However, for ultimate length and energy scaling this formula is no longer useful.

A laser power extraction model which includes distributed laser medium loss has been developed. This model can be used to predict the laser power extraction efficiency at optimum output coupling as a function of the small signal gain and absorption coefficients, g_0 and α , and the

laser length, L . The analysis assumes a stable optical resonator configuration in which the modes are assumed to be purely transverse. A homogeneously-broadened gain medium is also assumed. Since the laser pulse is much longer than the gain risetime and the photon transit time of the optical cavity, a steady state analysis was made.

The laser power extraction efficiency at optimum output coupling T was determined by solving a pair of simultaneous transcendental equations. The first equation determines the laser output flux, ϕ (normalized to the saturation flux) as a function of T , g_0 and α .

$$f(\phi, T) = \ell \ln \left[\frac{\frac{\phi}{T} - \frac{ra_+ + a_-}{2r}}{\frac{\phi}{T} - \frac{a_+ + ra_-}{2r}} \right] + \frac{1}{k} \left[2\alpha L + \ell \ln \frac{1}{r} \right] = 0 \quad (6)$$

where

$$\frac{1}{k} = 1 - \frac{\alpha}{g_0} \left[1 - \frac{4r\phi^2}{T^2 \left(\frac{g_0}{\alpha} - 1 \right)^2} \right]^{1/2}$$

$$a_{\pm} = \frac{1}{2} \left(\frac{g_0}{\alpha} - 1 \right) \left\{ 1 \pm \left[1 - \frac{4r\phi^2}{T^2 \left(\frac{g_0}{\alpha} - 1 \right)^2} \right]^{1/2} \right\}$$

$$r = 1 - T$$

A second transcendental equation in ϕ and T can be obtained by defining the extraction efficiency, η , as $\phi/g_0 L$, recasting the equation above as $g(\eta, T) = 0$ and forming

$$\left. \frac{\partial g}{\partial T}(\eta, T) \right|_{\frac{\partial \eta}{\partial T} = 0} = 0. \quad (7)$$

This transcendental equation can be solved simultaneously with Eq. (6) to give the extraction efficiency and normalized laser flux as the optimum output coupling for relevant values of $g_0 L$ and αL . These results are shown in Figures 7 and 8. In addition the optimum output couplings for these $g_0 L$ and αL values are plotted in Figure 9.

Note that for efficient extraction one must have $g_0 L \gg 1$, $\alpha L < 1$ and $g_0 > 10\alpha$. Now g_0 and α both depend on the level of excitation and laser mixture. α is also dependent on the laser cavity flux. For example, Kr_2F^* is an important absorbing species. Since Kr_2F^* is formed from KrF^* , it can be shown that with a laser cavity flux, the number density of Kr_2F^* is proportional to $1/(1 + \phi/\phi_{\text{sat}})$. The above analysis assumed that the absorber is nonsaturable; that is, the absorber density is not decreased by the laser cavity flux. This analysis can be used if one separates the total medium absorption into saturable (e. g., Kr_2F^* absorption) and nonsaturable (e. g., F_2 absorption) parts. The saturable part can be treated as an effective reduction in small signal gain g_0 , as long as

$$\alpha_{\text{sat}} \sim \frac{1}{1 + \phi/\phi_{\text{sat}}} \quad (8)$$

The analysis is then used with an effective small signal gain $g_0 - \alpha_{\text{sat}}$ inserted.

To calculate laser efficiency and scaling, the extraction model can be coupled to the kinetics calculations. This has been done and an example of the result of such a calculation for a 1-meter KrF^* laser pumped by a 11.5 A/cm^2 , 250 kV, 600 nsec e-beam is shown in Table 2.

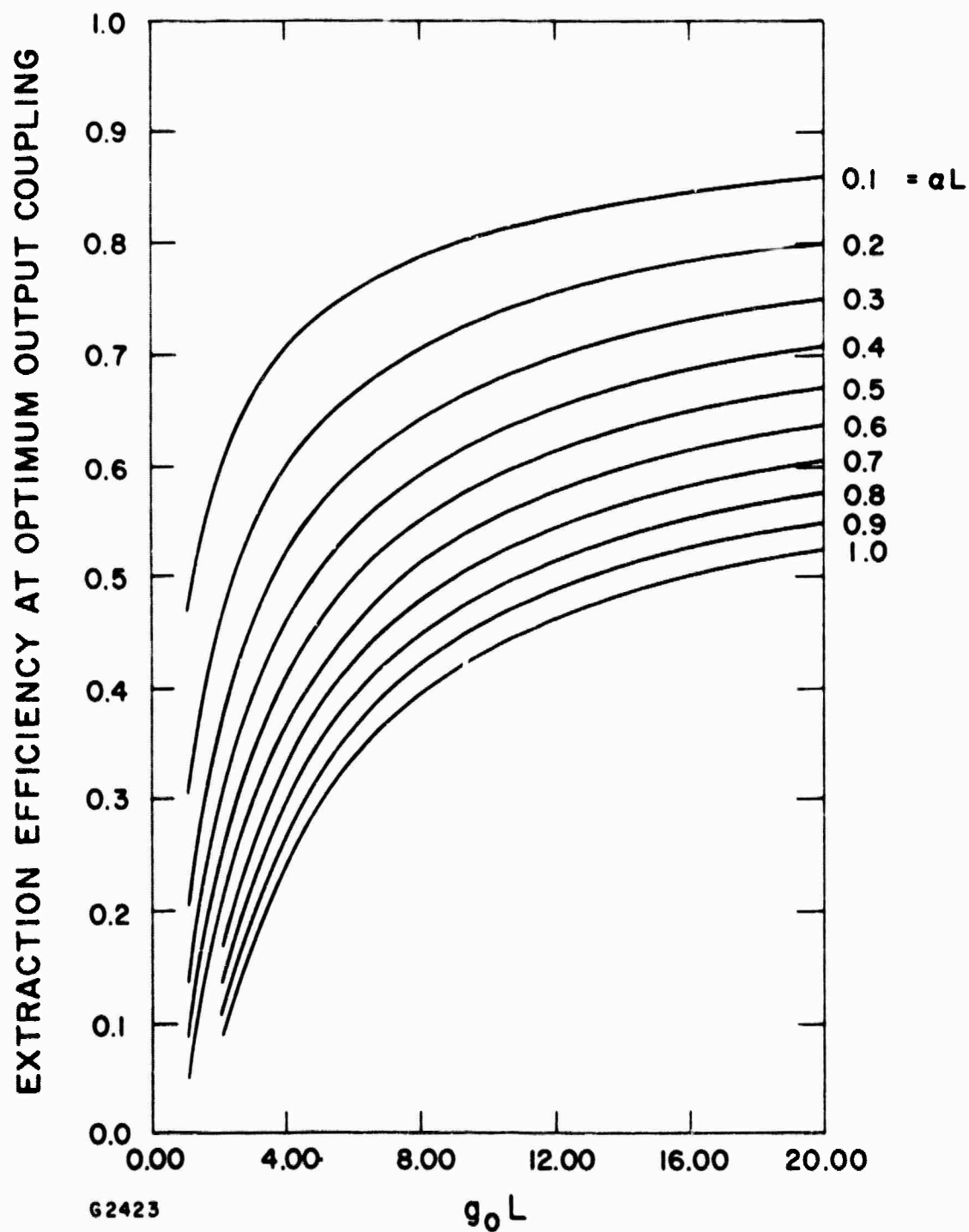


Figure 7 Laser Power Extraction Efficiency at Optimum Output Coupling Plotted against $g_0 L$ with aL as a Variable Parameter

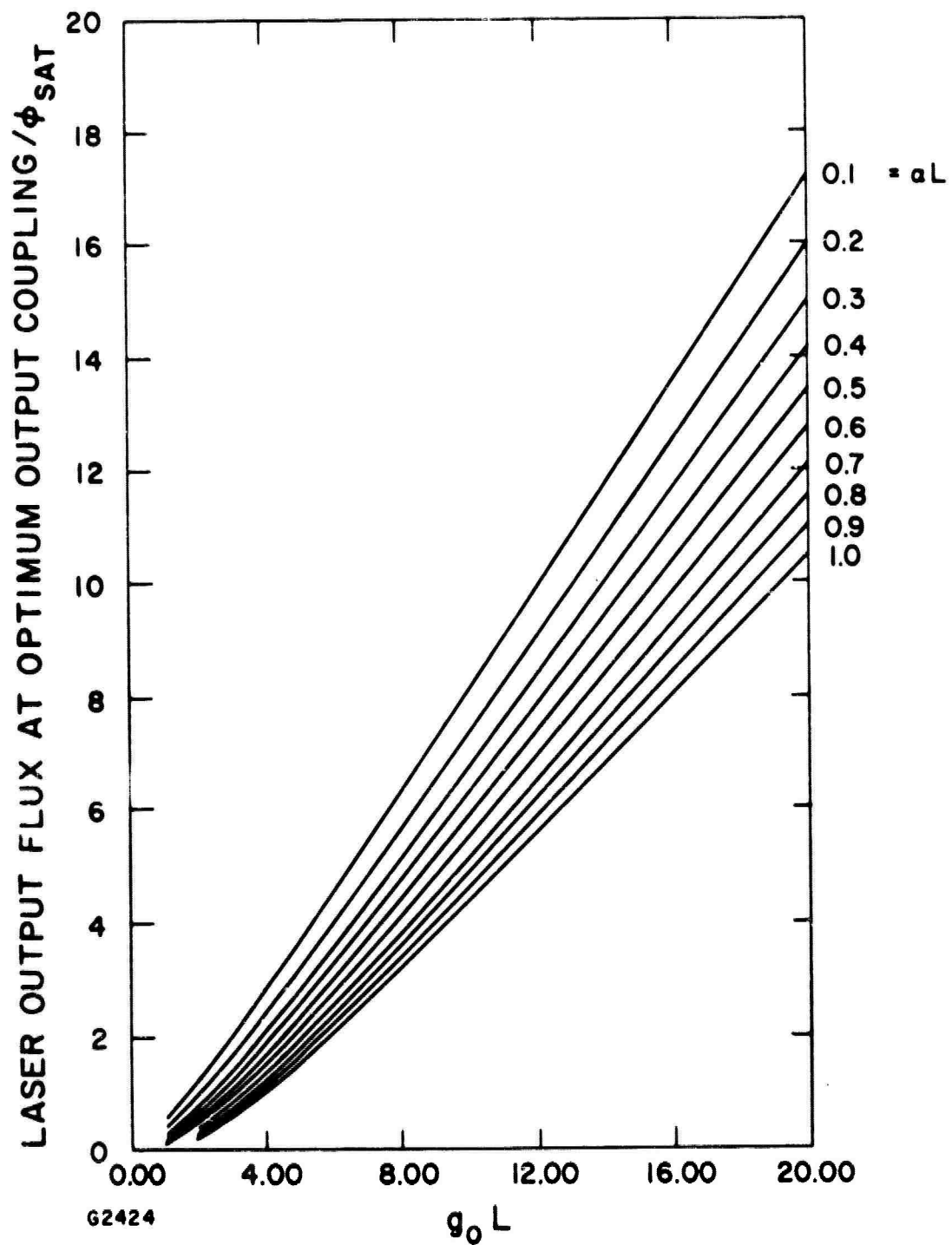


Figure 8 Laser Output Flux Normalized to the Saturation Flux Plotted as a Function of $g_0 L$ with aL as a Variable Parameter

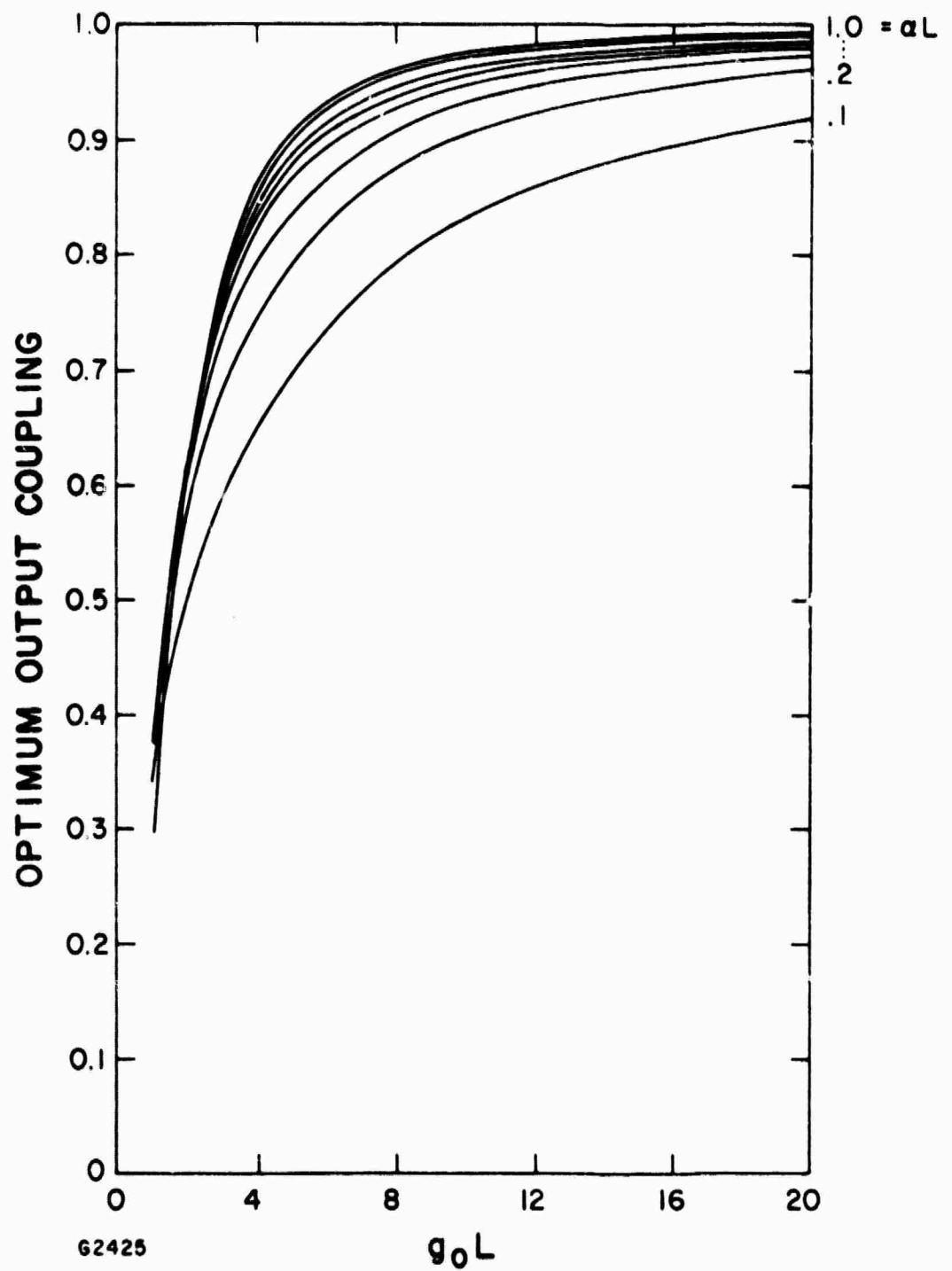


Figure 9 Optimum Output Coupling as a Function of g_0L and αL

TABLE 2
KrF^{*} LASER MODEL PREDICTIONS

Laser Mixture	0.2%F ₂ /4% kV/95.8% Ar @ 1.7 atm
E-Beam Energy	250 kV
E-Beam Current Density	11.5 amps/cm ²
Pulse Length	600 nsec
Length of Active Medium	1 meter
Laser Optical Cavity Output Coupling	70%
Small Signal Gain (g ₀ L)	3.3
Laser Medium Absorption at 249 nm	0.34
Laser Cavity Flux (ϕ_{cav})	3.7 MW/cm ²
Saturation Flux (ϕ_{sat})	1.4 MW/cm ²
ϕ_{cav}/ϕ_{sat}	2.6
KrF [*] Stimulated/KrF [*] Formed	0.73
Extraction Efficiency (Laser Photons Out/KrF [*] Formed)	46%
Energy Extraction	12.6 J/liter
Intrinsic Laser Efficiency (Laser Output Energy/Energy Deposited)	9.8%

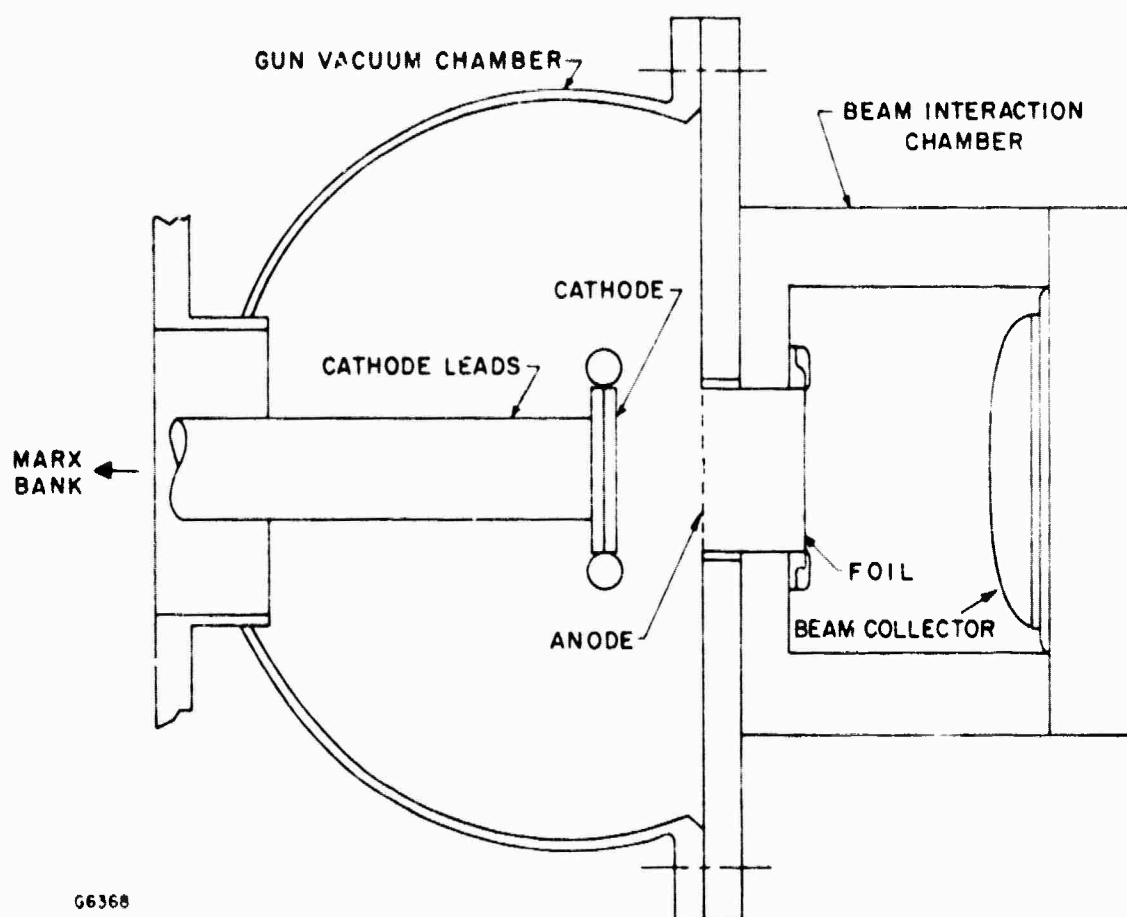
IV. ONE-METER E-BEAM/E-BEAM SUSTAINED DISCHARGE DEVICE

To demonstrate efficient large pulse energy extraction and test our scaling prediction, a one-meter device was designed and built. A cross-sectional view of the cold cathode e-gun is shown in Figure 10. The e-gun was designed to generate a beam with the following characteristics:

Beam Energy	250-350 keV
Current Density	$\leq 10 \text{ A/cm}^2$
Area	10 cm x 100 cm
Pulse Length	$\geq 1 \mu\text{s}$

The gun is powered by a 5-stage Marx generator built by Maxwell which is connected to the cathode through 2 parallel high voltage vacuum bushings to minimize circuit inductance. The cathode lead current is monitored by two current transformers mounted outside the bushing.

Both graphite and tantalum blade cathodes have been used; however, for fast current rise, tantalum blade cathode is generally chosen. The blades are two mil thick tantalum strips, each 1 meter long. A picture of the cathode and the e-gun chamber is shown in Figure 11. The anode is made of 75% transparent stainless steel screen. After the anode screen there is a 4 cm long field-free drift region. The electron beam enters the laser cavity through a 2-mil thick aluminized kapton foil which is supported against the pressure in the laser cavity by a 90% open "hibachi" support structure. The e-gun chamber is pumped by a 6-inch baffled diffusion pump backed by a 15 CFM mechanical pump. Typical operating pressure in the e-gun is $\approx 10^{-5}$ torr.



G6368

Figure 10 Cold Cathode E-Gun

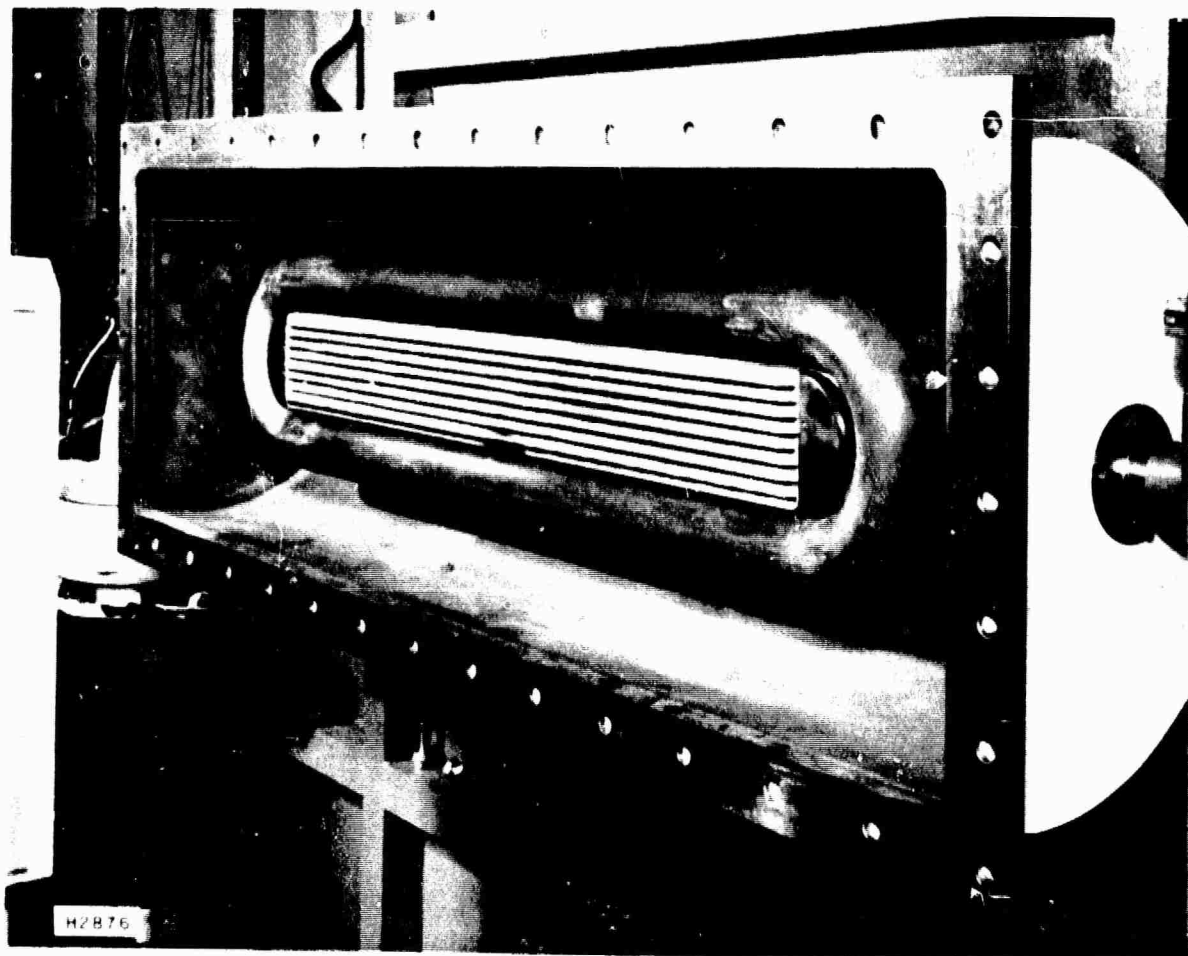


Figure 11 Photograph of the Cathode and E-Gun Chamber

The Marx generator circuitry is shown in Figure 12. The Marx bank consist of 5 capacitors ($1.25 \mu\text{F}$, 75 kV) and the bank is erected by 5 series triggered spark gaps. The bank is connected to the cathode lead through 2Ω resistors ($\text{H}_2\text{O} + \text{NaCl}$) which dissipate the Marx energy in the event of an arc over in the e-gun or bushing. In addition, these resistors aid in complete voltage (and current) crowbarring by the diverter gap. Typically at most one quarter of the stored energy in the bank is used in the e-gun. The remaining energy is crowbarred by a diverter gap. Therefore, the voltage droop during the e-gun pulse is small, typically less than 15%. This allows reliable diverter operation and minimizes the number of low energy electrons striking the foil. The diverter and series gaps are triggered, through trigger generators, by two sequential pulses. Variable delay between the pulses allows e-beam pulse widths to be varied from 200 nsec to $1.5 \mu\text{sec}$.

A cross-sectional view of the laser cavity is shown in Figure 13. The cavity is constructed of plexiglass and has a G10 strongback. This allows cavity pressures of up to 5 atm. The laser optical cavity is formed by two mirrors external to the laser cavity. Generally a flat-flat optical cavity is used so that the intensity variation across the laser output beam directly reflects the variation in e-beam or discharge energy deposition.

For e-beam sustained discharge pumping a stainless steel screen is placed 2 cm in front of the foil. This screen serves as the grounded discharge cathode. A stainless steel discharge anode is placed 10 cm from the foil. This anode also serves as an e-beam collector plate. The discharge anode is connected to discharge circuitry by three feedthroughs to



45

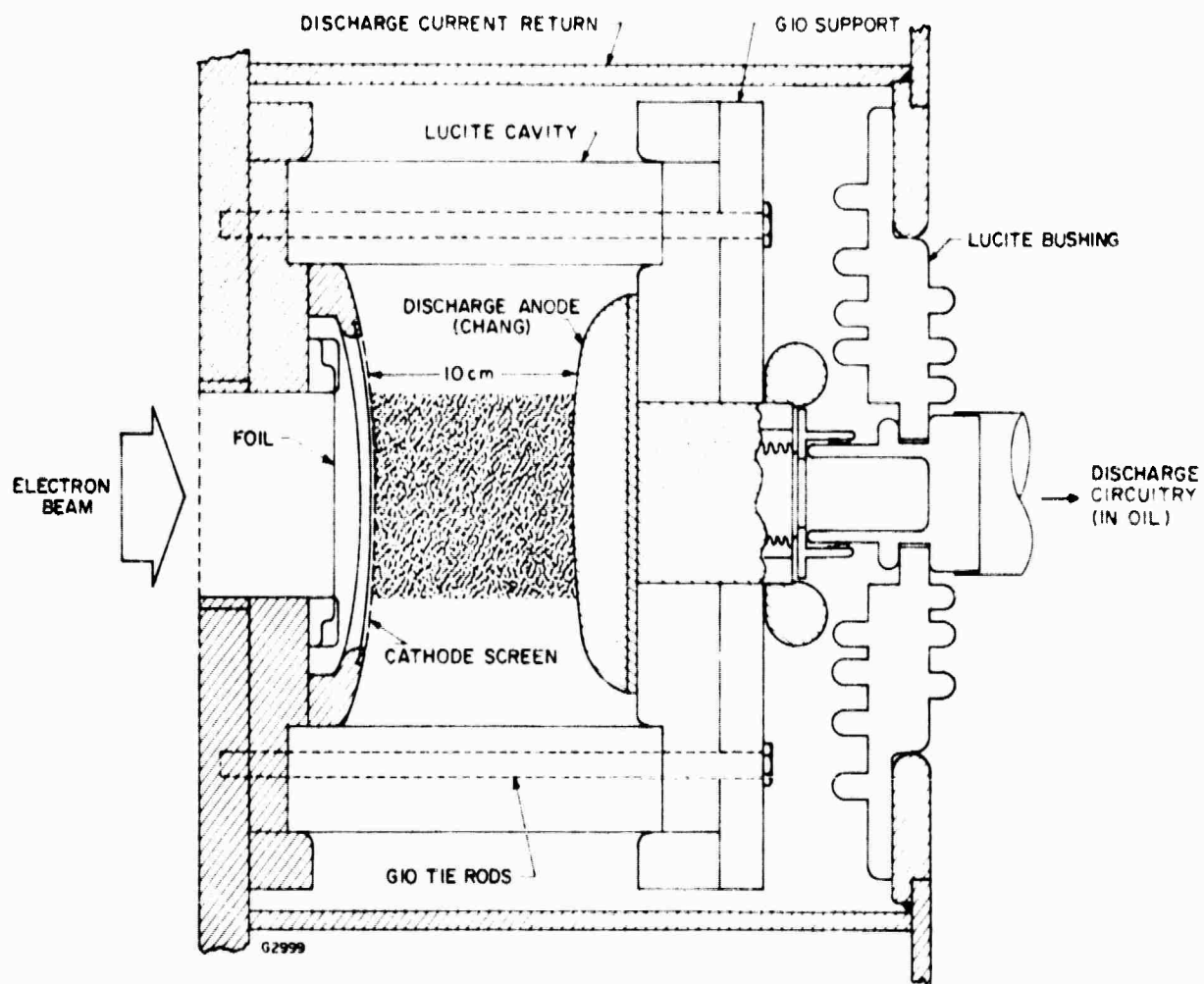


Figure 13 One Meter KrF Laser Cavity

minimize inductance. Discharge current is monitored by 3 current transformers in the return path, and the discharge voltage is monitored by a $20\ \Omega$ $\text{H}_2\text{O}/\text{CuSO}_4$ resistor connected from anode to ground through a current transformer.

The discharge circuitry is contained in a separate oil tank. A schematic of the discharge circuitry is shown in Figure 14. This low inductance circuit allows discharge voltages of up to 100 kV which corresponds to electric field of up to 10 kV/cm at full anode-cathode spacing. A triggered series rail spark gap connects the capacitors across the discharge electrodes through three parallel $\text{H}_2\text{O}/\text{CuSO}_4$ resistors. These resistors dissipate the energy in the event of an arc in the discharge and also allow the remaining capacity energy to be crowbarred by a diverter gap after the desired pulse duration has been reached. This allows the discharge voltage to be held at the desired value over the entire discharge pulse. This circuitry allows us to explore a range of operating conditions. Once the optimum has been found however, this circuitry can be replaced by a PFN to give optimum performance and efficiency.

The discharge circuitry, the e-gun together with the Marx generator, and the laser cavity together with the vacuum system are mounted on three separate carriages, each riding on rails so that they can be separated for easy access into the e-gun and laser cavity. A photo of the entire system is shown in Figure 15.

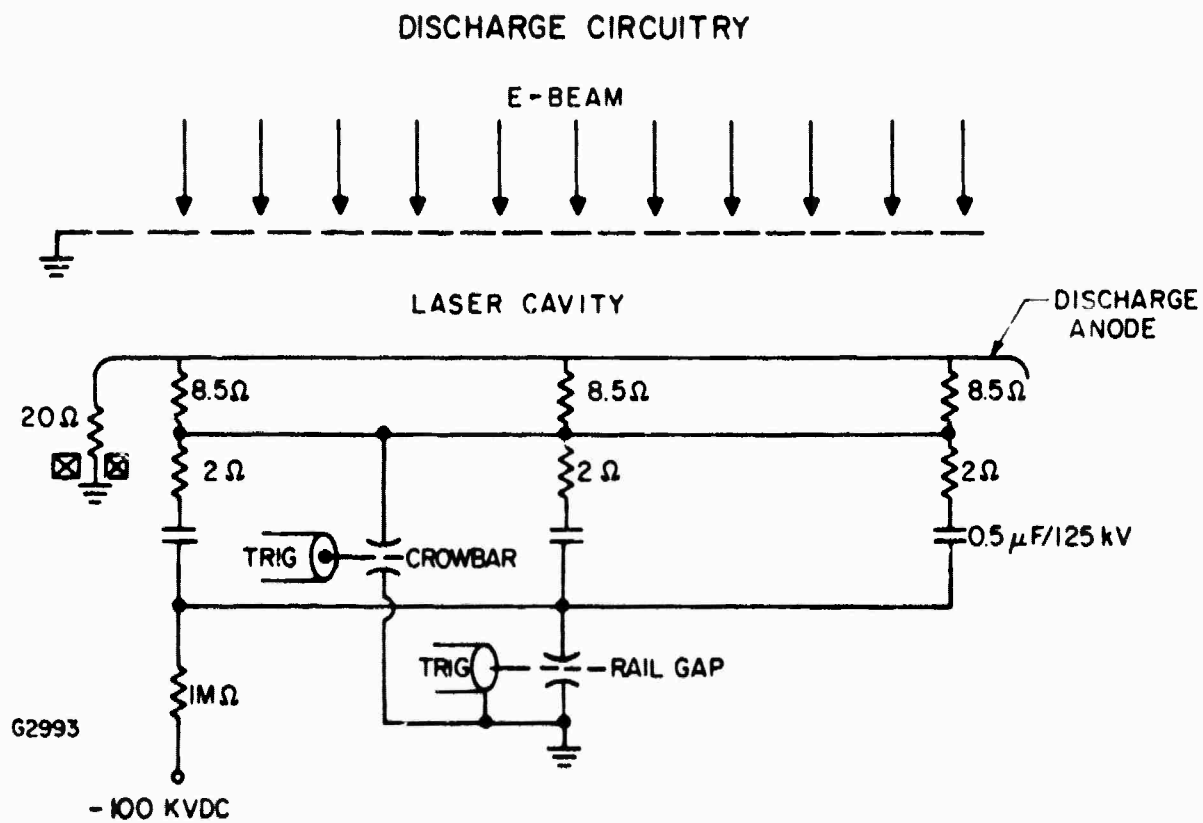


Figure 14 One Meter KrF Laser Discharge Circuitry

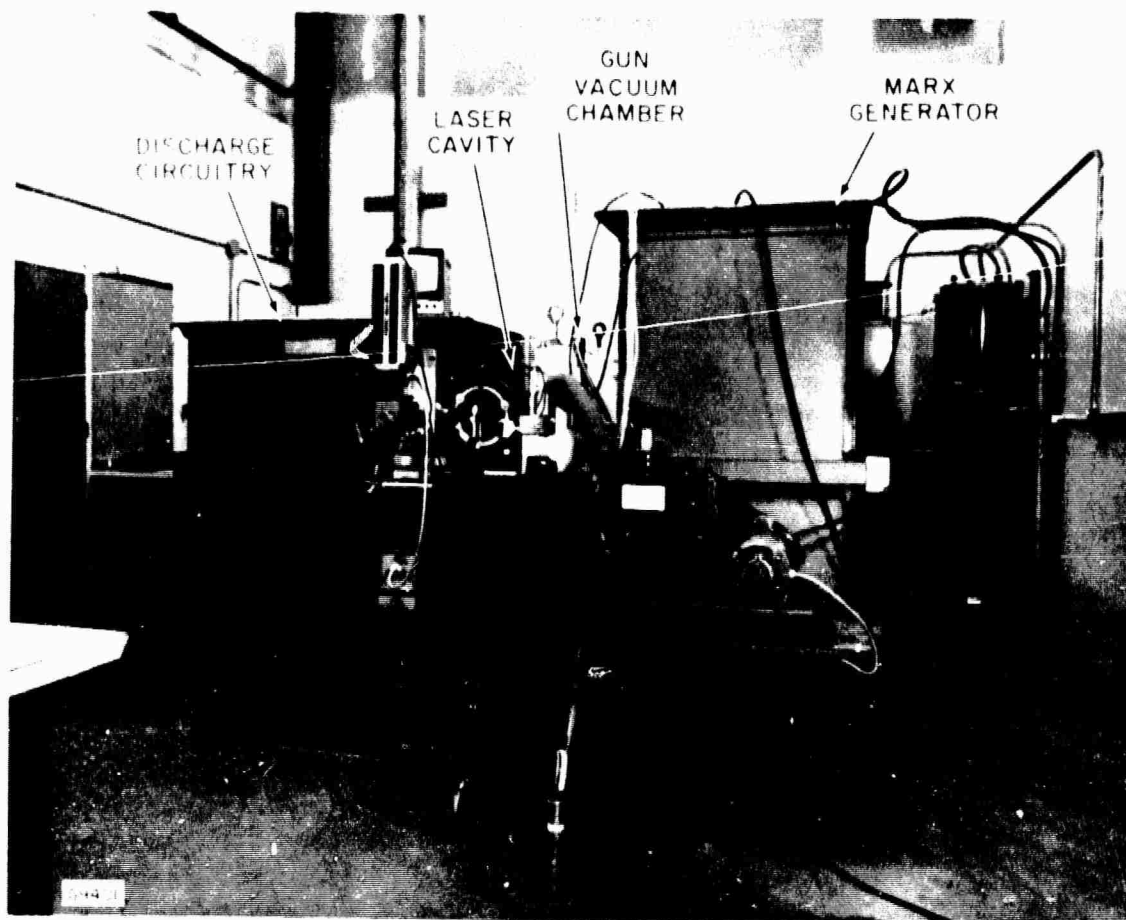


Figure 15 Photograph of Entire Device

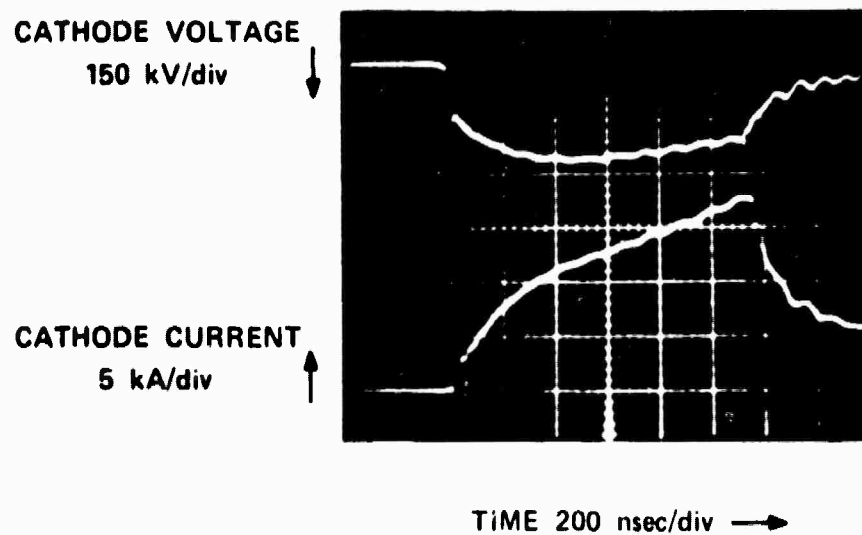
V. E-BEAM MEASUREMENTS AND INITIAL KrF* LASING EXPERIMENTS

After some initial system checkout and characterization a series of e-beam characterization experiments were performed. An example of e-gun cathode lead voltage and current traces are shown in Figure 16. The 200 nsec risetime in the voltage was caused by Marx generator circuit inductance and the final voltage droop was due to the draining of the capacitors. The lead current rose continuously during the entire pulse because of diode closure.

The transmitted e-beam in the laser chamber was measured as a function of position along the plane of the foil and along the direction away from the foil. Three different diagnostic techniques were used.

(1) Time integrated e-beam intensity variation in the plane parallel to the foil was measured by placing strips of Cinamoid in the path of the e-beam. Cinamoid is a red gel, encapsulated in plastic, which becomes bleached by the action of the e-beam. The light transmission through the film after e-beam exposure is a measure of integrated e-beam current density in coulombs/cm². The response (transmission/e-beam exposure) was not quite linear in the range of exposures provided by our device in a 1 μ s pulse. The great advantage of this technique is that an approximate e-beam spatial profile can be taken quickly with a single pulse.

(2) Time resolved e-beam profiles were also measured using a collimated photodiode which measured the KrF* fluorescence intensity emerging from the laser cavity. The experimental arrangement used is



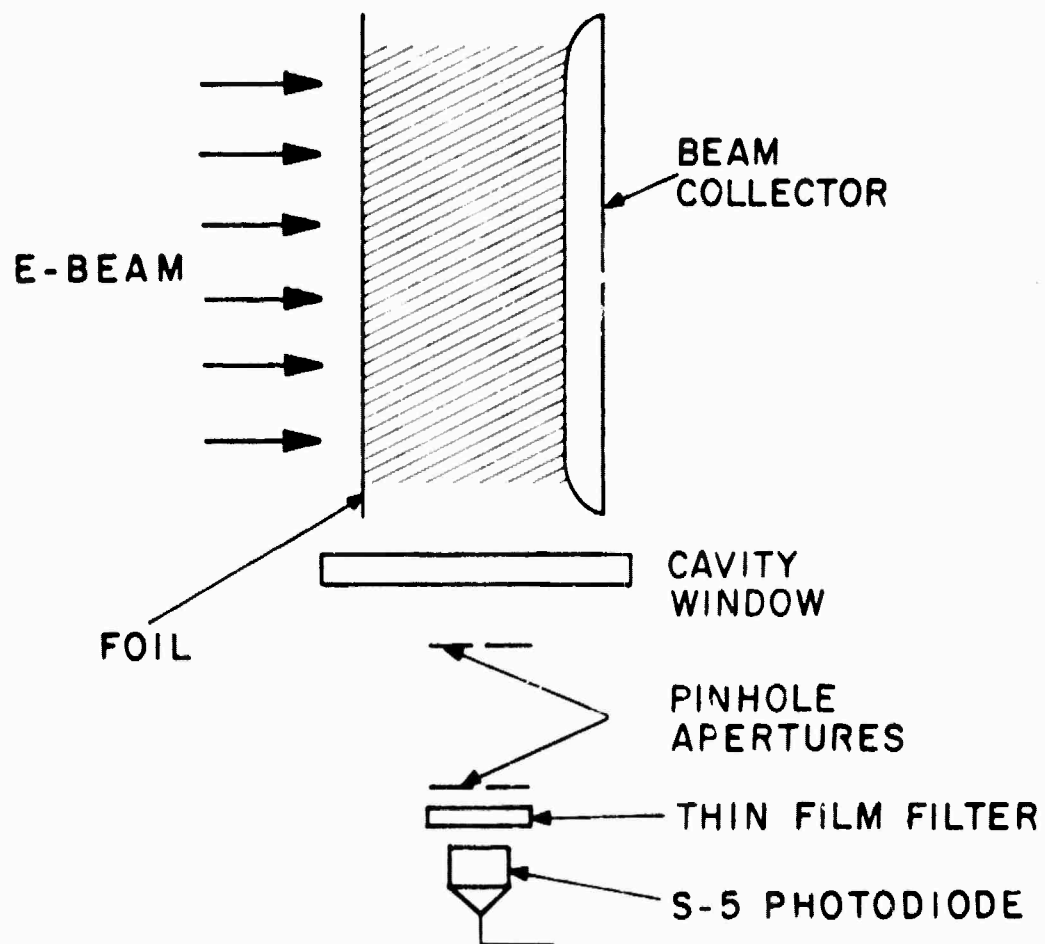
H2878

Figure 16 E-Gun Cathode Voltage and Current Characteristic

shown in Figure 17. Pinholes aligned parallel to the laser optical cavity axis were used in front of the photodiode so that only collimated light reached the detector. The pinhole and detector assembly were mounted on linear translation stages so that scans could be made across the plane of the cavity window. For those measurements, 248 nm fluorescence in mixtures of Ar, F_2 and Kr were used. The medium was optically thin, therefore, the detector saw fluorescence averaged over the length of the cavity. Therefore, only e-beam deposition variations across the laser aperture were monitored.

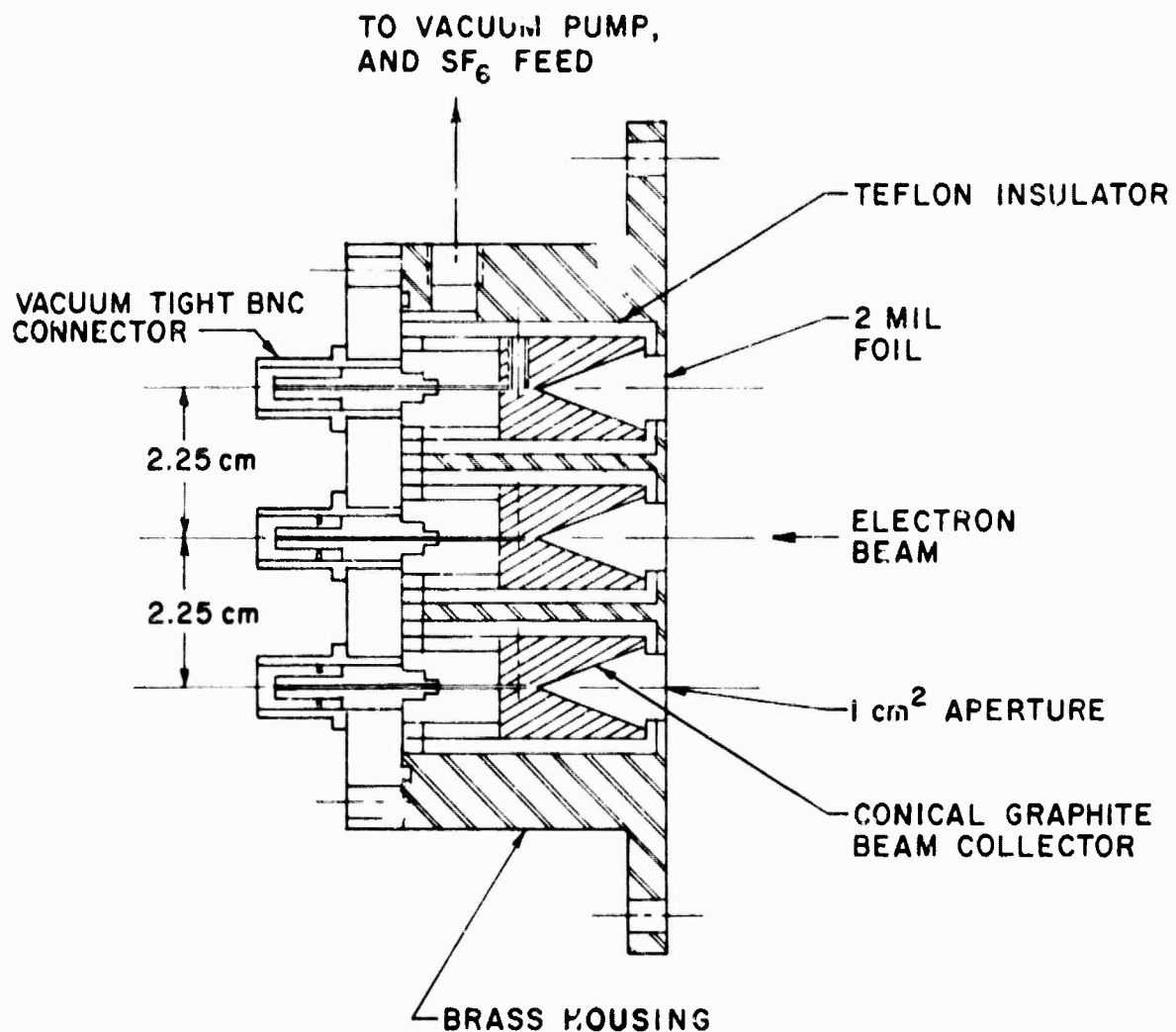
(3) The e-beam intensity was also measured with a Faraday cup array. The design of the array is shown in Figure 18. Each element collected 1 cm^2 of the e-beam. Conical graphite collectors were used to minimize electron reflection. Each element was fed into a coaxial cable matched at the oscilloscope for fast temporal response. The array was filled with SF_6 to prevent breakdown and plasma return current flow.

An example of the transverse beam profile taken with Cinamoid strips are shown in Figure 19. These are vertical scans (across the short direction) taken 0.5 cm from the face of the foil. The top trace was taken at 6 cm e-gun anode-cathode spacing at 300 kV applied which corresponded to an averaged transmitted current of 8 A/cm^2 . The bottom trace was taken with 8 cm anode-cathode spacing at 300 kV which corresponded to an averaged transmitted current of 5 A/cm^2 . Note the effect of beam pinching. At only 0.5 cm from the foil, the effect of beam scattering by the foil and gas was small; therefore, the center to edge beam fall off was due strictly to the pinching of the beam by its self-magnetic field occurring in the vacuum diode and drift regions. The effect became more pronounced



H2879

Figure 17 E-Beam Energy Deposition Measurement Apparatus



G6735

Figure 18 The Beam Collectors in the Faraday Cup Array are Constructed from Graphite to Minimize Albedo. Each collector is terminated in 50 Ω and the voltage across these resistors are monitored. The Faraday cup array is typically evacuated and backfilled with ~ 100 torr of SF_6 to eliminate plasma return current effects.

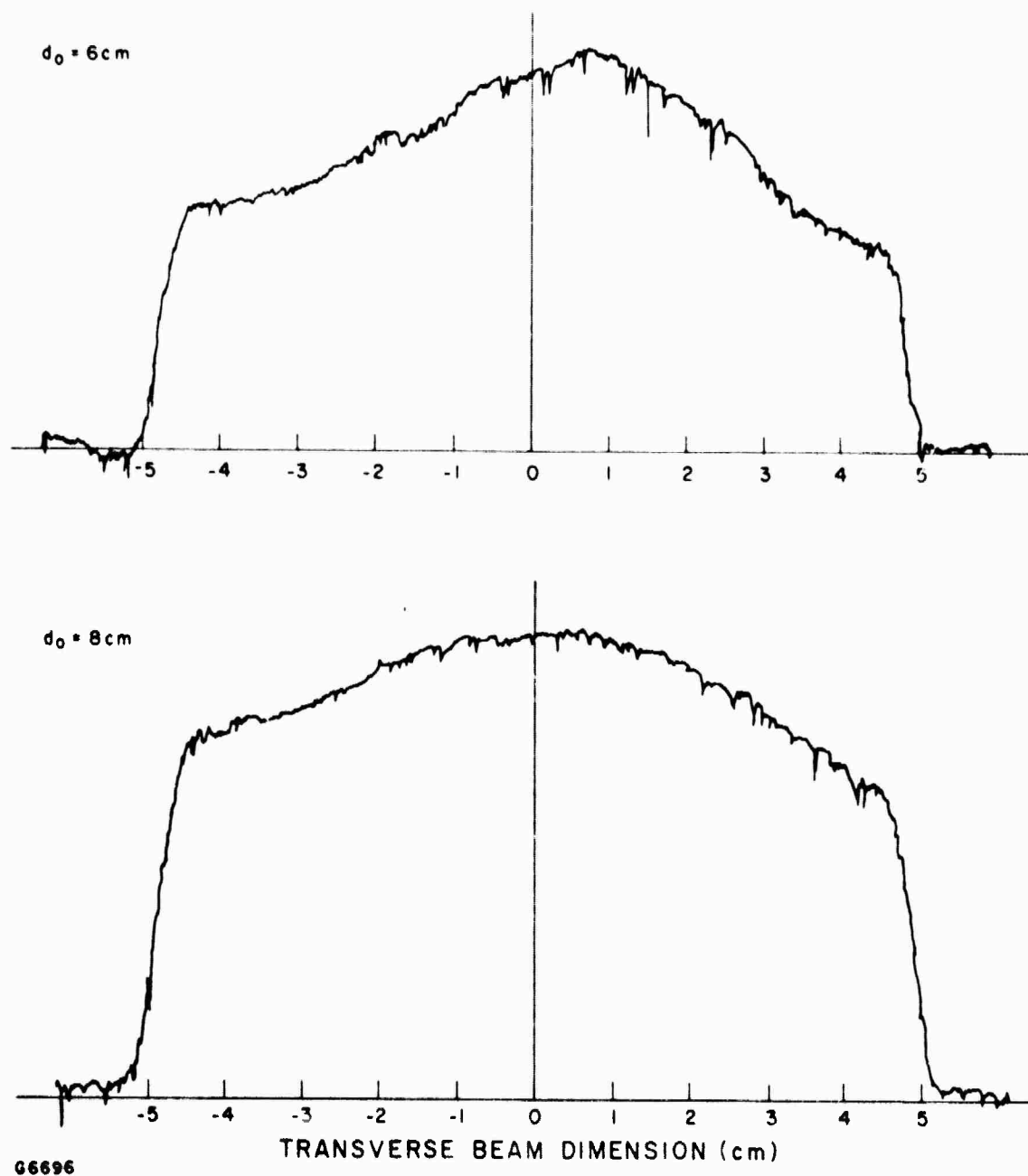
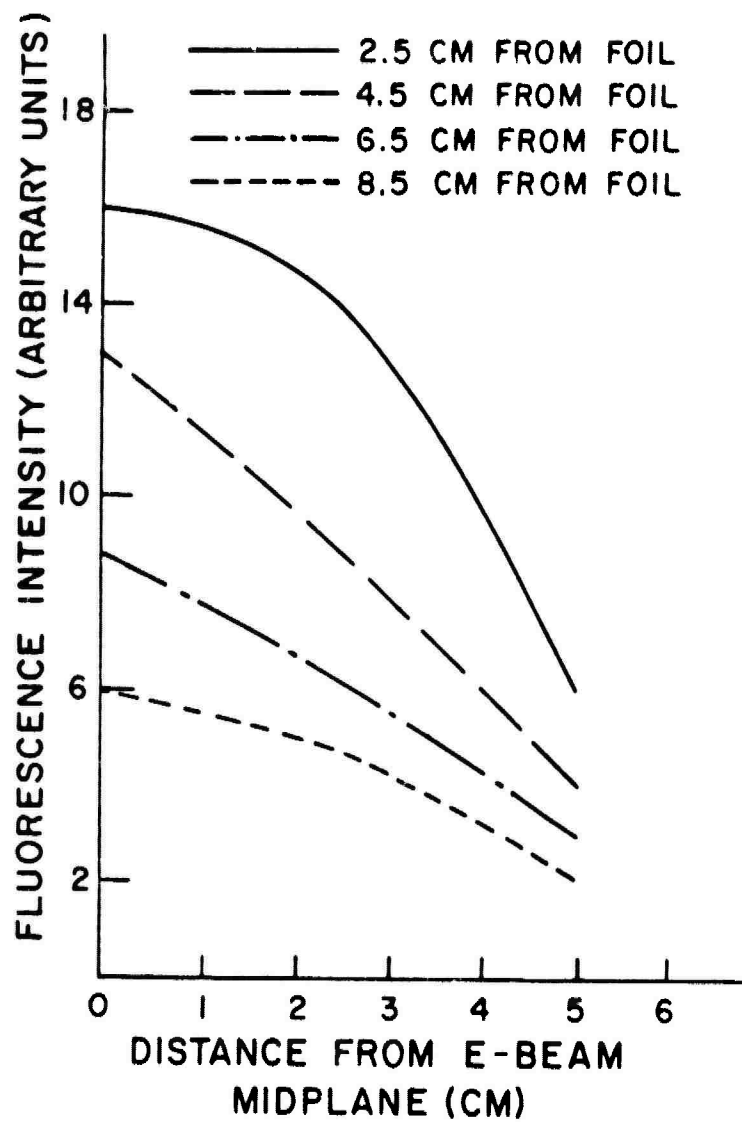


Figure 19 Transverse Beam Profiles for Gun Anode-Cathode Spacings of 6 and 8 cm

as the beam current was raised. Here we see almost a factor of two variation in beam intensity from the center of the foil to the edges for the 6 cm anode-cathode spacing case.

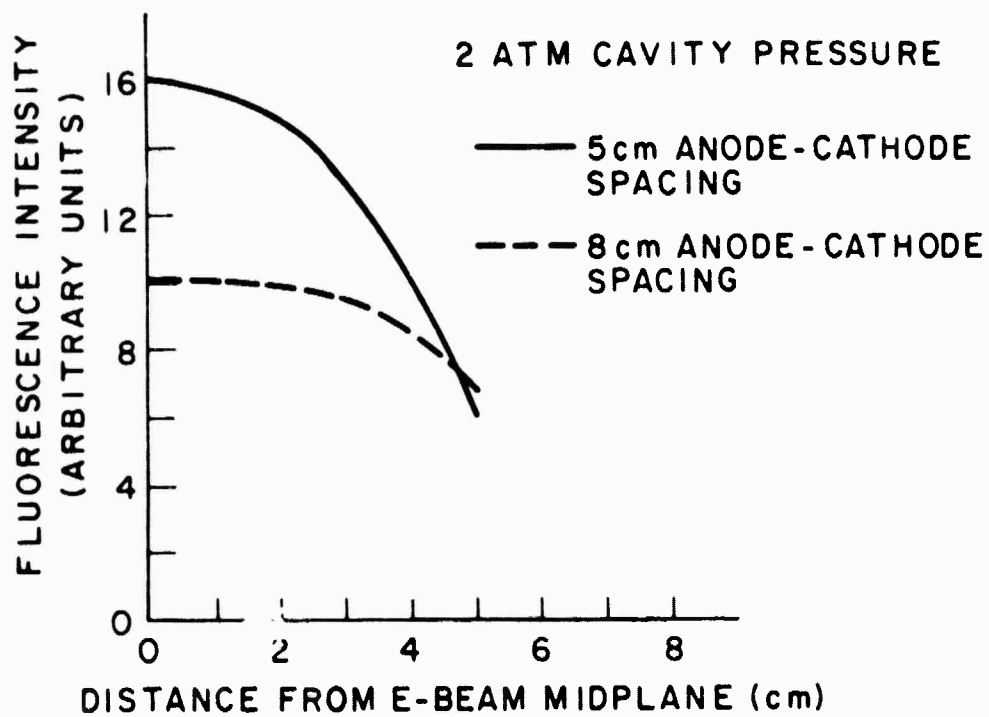
More quantitative data were obtained using the fluorescence technique. Examples of the results of these measurements are shown in Figures 20 and 21. Figure 20 shows vertical scans made at various distances from the foil with 2 atm cavity pressure and 5 cm e-gun anode-cathode spacing. Note at 2.5 cm from the foil, the variation in e-beam energy deposition across the short e-beam dimension was almost 3 to 1. There are two contributing effects in this case. Beam pinching before the foil in the e-gun chamber and spatial beam diffusion caused by small angle scattering in the foil and in the 2 atm gas mixture. Moving downstream of the e-beam away from the foil, stopping of the e-beam by the gas mixture, caused additional falloff in e-beam deposition. Here the effects of beam scattering and stopping combined to yield a factor of 2.7 falloff in e-beam energy deposition while traversing only 6 cm down the cavity mid plane. For this case the total variation from the point closest to the center of the foil to the furthest point within the cross section defined by the laser optical cavity was greater than 10 to 1. Figure 21 compares the vertical beam deposition variation at 2.5 cm from the foil for two different e-gun anode-cathode spacings.

Time resolved and spatially localized transmitted e-beam current was measured with the Faraday cup array. An example of a resulting oscilloscope trace is shown in Figure 22. Here the array was placed with the Faraday cup apertures 1/2 cm away from the face of the foil. The e-gun anode-cathode spacing was 7.5 cm and the Marx voltage was 300 kV. The



H2880

Figure 20 Vertical Fluorescence Intensity Scans at Various Distances from the Foil



H2881

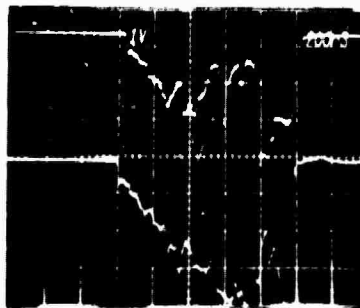
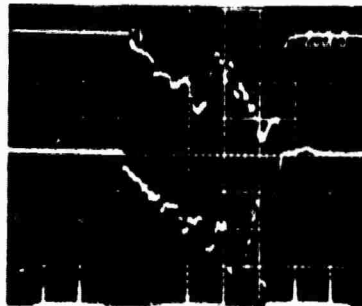
Figure 21 Vertical Fluorescence Intensity Seen with Various E-Gun Anode-Cathode Spacings

BEAM CURRENT DENSITY
(1 cm² AREA)
A-K SPACING = 7.5 cm
ANODE SCREEN

2.25 cm UP FROM
BEAM CENTER

BEAM CENTER

SENSITIVITY
2.3 A/cm²/div



TIME →
200 ns/div

G7110

Figure 22 Beam Current Density Variations in the Maxwell E-Gun. Data, which are from three consecutive shots, show the stochastic nature of these fluctuations.

three sets of traces shown are results of three successive shots taken under identical conditions. Signals from two Faraday cups are shown. The bottom traces show signals from the cup centered at the foil midplane and the top traces are those from one centered 2.26 cm above the midplane. Here we see large amplitude beam intensity fluctuations taking place on 10 nsec time scales. Note that locally the beam intensity can change by a factor of 2 in times of order of 25 nsec. We believe that fast fluctuations are caused by localized ion emission from the e-gun anode (bipolar diode effect) backstreaming under the electric field causing enhanced electron emission at the cathode. A theoretical discussion of this will be presented in Appendix A.

For pure e-beam pumping the effect of the localized fast temporal e-beam fluctuations is minimized by the spatial averaging over the length of the laser by the laser cavity flux. However, the effect of the large scale nonuniformities in energy deposition over the laser aperture can be serious indeed. We have shown, in the previous section, that for a given level of excitation there is, for optimal energy extraction, an optimal laser gas mixture and also an optimal cavity flux (optical cavity output coupling). Nonuniformity in excitation over the laser aperture will mean that this optimal condition can only be chosen for a small portion of the entire laser aperture. For a given output coupling, the intensely excited region would be undercoupled, leading to inefficient extraction due to higher than necessary laser medium absorption losses while the less intensely excited regions will be insufficiently saturated or worse still, the excitation may not be sufficient to reach threshold. A carefully designed unstable laser cavity

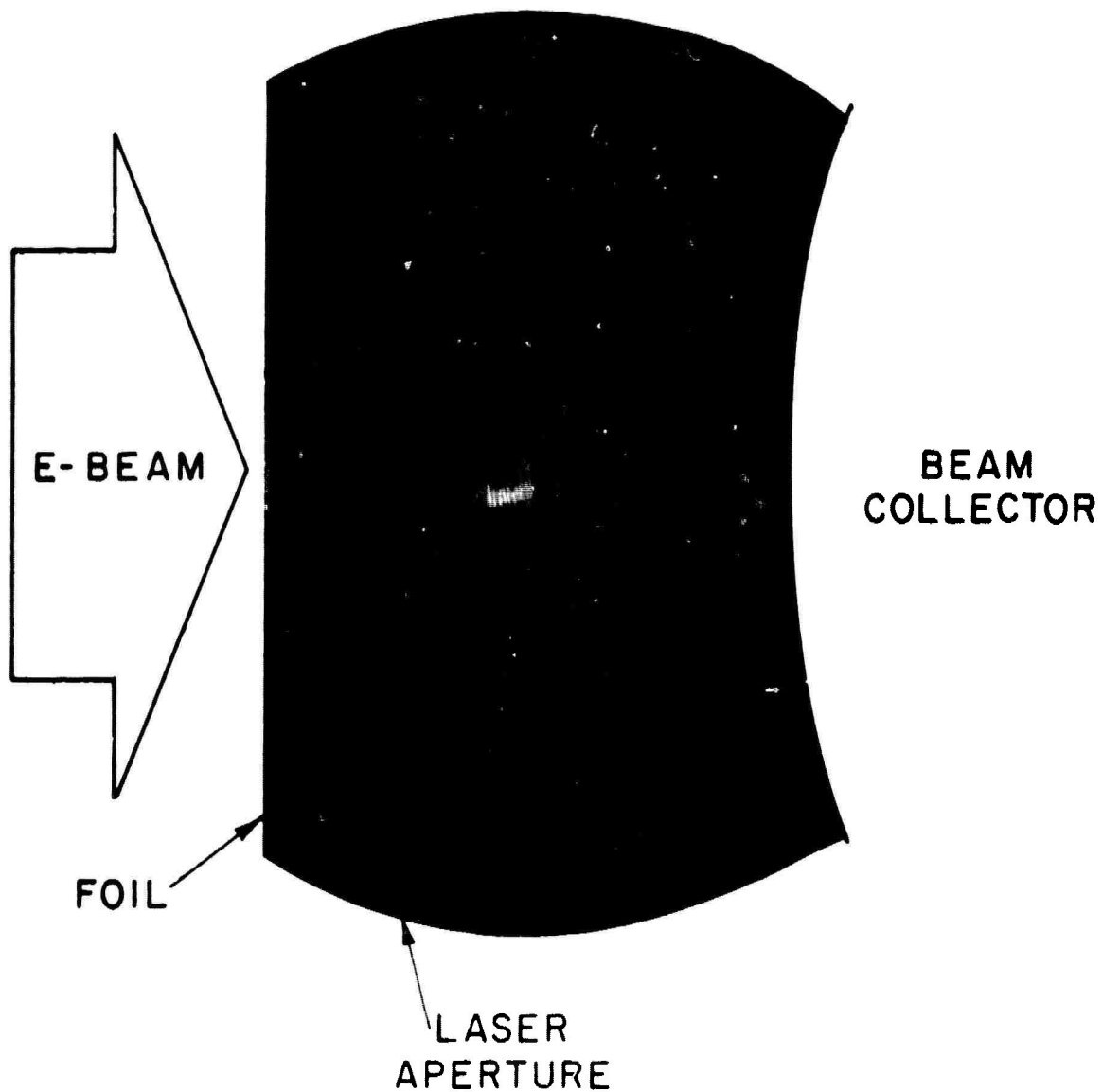
would partially alleviate this problem; however, for optimum energy extraction per unit laser volume uniform excitation must be maintained.

Even though it was realized that with the measured nonuniformity in e-beam energy deposition, efficient energy extraction would not be possible over the entire laser aperture, KrF* lasing experiments were carried out so that comparisons can be made when improvements in e-beam uniformity are achieved. The experimental conditions and major results are summarized below:

Laser energy out	25 joules
Intrinsic laser efficiency	3%
Active laser volume	10 liters
Energy extracted per liter	2.5 joules/liter
Output pulse length	1 μ sec
e-beam energy	300 kV
Average e-beam current	10 A/cm ²
Laser mixture	0.2% F ₂ /5% Kr/94.8% Ar at 1.5 atm

A laser beam burn pattern is shown in Figure 23. Note that as expected, efficient lasing occurred only over a small portion of the laser aperture and the energy output and efficiency were low compared with those predicted theoretically when uniform excitation was assumed. An encouraging fact shown by these experiments is that if we take the laser volume to be that indicated by the size of the burn pattern, then the calculated energy extraction from this reduced volume is close to the 10 joule/liter predicted.

KrF* LASER BURN PATTERN



DIRECT ELECTRON BEAM PUMPING

H2882-1

Figure 23 KrF* Laser Burn Pattern (No Magnetic Field)

VI. E-BEAM CONFINEMENT BY EXTERNALLY APPLIED GUIDE FIELD

In the e-gun the magnetic field generated by e-beam current flow can cause the beam to pinch on itself. The magnitude of this effect can be estimated by calculating the Larmor radius at the electron under the influence of its self field. For an initially uniform e-beam of current density J having height h and width w such that $w \gg h$, the magnetic field, B , at the edge of the beam is given by

$$B = \mu_o J_{eb} \frac{h}{2} \quad (9)$$

The Larmor radius r_L for the edge electrons is then given by

$$r_L = \frac{\mu}{eB} = \frac{2\mu}{e \mu_o J_{eb} h} \quad (10)$$

where μ is given by

$$\mu = (2m_o E)^{1/2} \left(1 + \frac{E}{2m_o c^2}\right)^{1/2} \quad (11)$$

and m_o is the electron rest mass and E is the electron energy. In Figure 24 we have plotted the self-magnetic field and the Larmor radius for an edge electron versus the quantity $J_{eb}h$. If we take for our e-beam $J = 10 \text{ A/cm}^2$ and $h = 10$ we get $r_L \approx 30 \text{ cm}$ and in going from the cathode to the foil ($\approx 9 \text{ cm}$) the edge electrons will have moved 1.5 cm towards the center of the beam. Therefore, the effect will be quite pronounced. From Figure 24 we see that if the beam is allowed to pinch, height scaling of the e-beam would be severely limited.

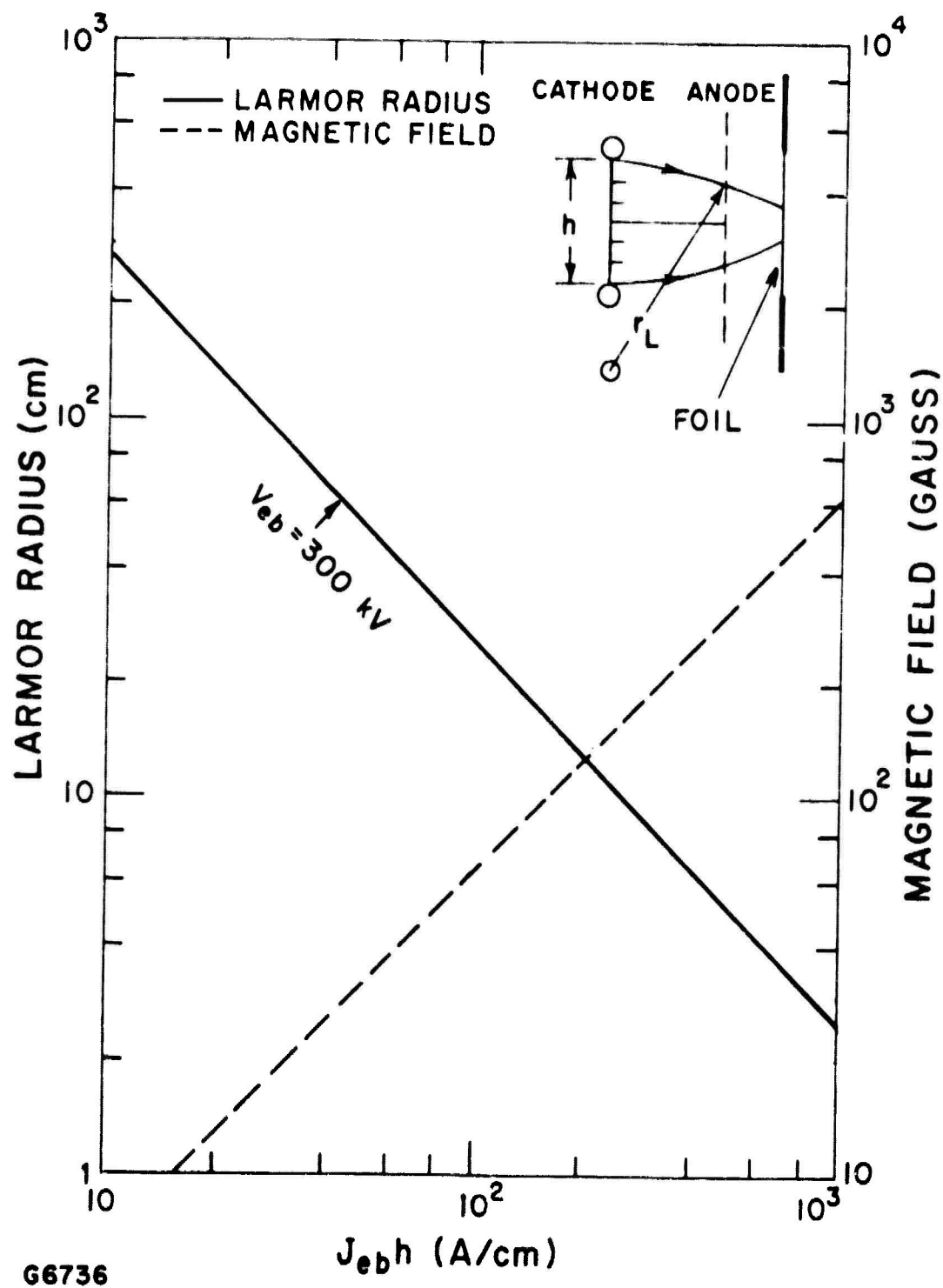


Figure 24 The Larmor Radius of a Beam Electron at the Gun Anode is Plotted Against the Product of Beam Current Density and Beam Height. The magnetic field seen by the edge beam electrons is also plotted.

Scattering and slowing of the e-beam by the foil and high pressure laser mixture leads to spatial diffusion of the e-beam and falloff in e-beam energy deposition as one moves away from the foil. These effects can be calculated by using a two-dimensional age theory (see Appendix B). We have done this for an initially uniform 300 kV, 10 cm high e-beam, impinging on a 2 mil Kapton foil, then entering a 1.7 atm Argon-filled region. The result of such an analysis is shown in Figure 25, where we have plotted contours of constant e-beam energy deposition in the gas. Note that the energy deposition decreases in every direction as one moves away from the center of the foil. Here we see a factor of 2.5 falloff at the center of the beam going from the foil to the far side of the cavity. When the effect of beam pinching in the e-gun is taken into account the calculated e-beam deposition profile agrees quite well with the measured fluorescence variations reported in the previous section.

Both beam pinching and transverse beam diffusion can be arrested by the use of an externally applied magnetic guide field. If we apply a magnetic field in the direction of e-beam current flow with intensity much greater than the e-beam's self field, then the scattered electrons will follow tight helical orbits around the applied field lines. The electrons can stray from a field line by only one Larmor radius, which is given in this case by

$$r_L = \frac{mV_{\perp}}{eB} \quad (12)$$

where B is the external field strength and V_{\perp} is the component of the electron velocity in the plane perpendicular to B . Before entering from the foil V_{\perp} is small and the electrons follow the field lines closely. Scattering gives

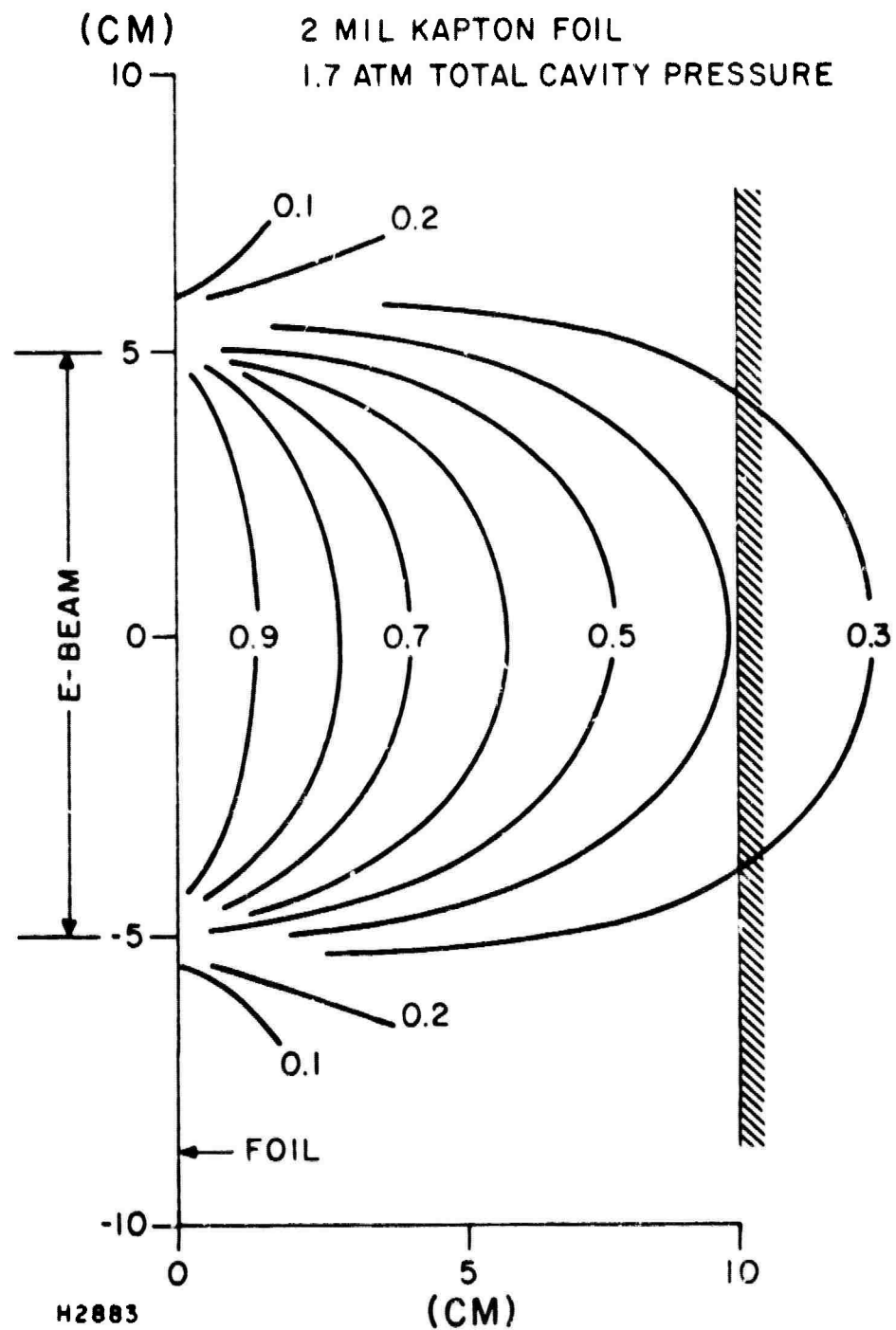


Figure 25 Calculated Contours of Constant E-Beam Energy Deposition without External Magnetic Field

rise to V_1 and downstream from the foil the beam will spread slightly. The spreading will be of order r_1 . With sufficient applied field the spreading can be made negligible.

In Figure 26 we have again calculated the e-beam energy deposition profile for conditions identical to that of Figure 25, except here we have assumed a uniform applied field of 800 G. In this case one sees that the beam is effectively confined and the energy deposition is uniform in the transverse direction for all but the 1 cm near the far edge of the beam. In the beam direction the energy deposition is now peaked inside the laser region. This simply is due to the increase in the stopping power of the gas as the e-beam slowed in the gas. Here the e-beam energy deposition is uniform, to within a factor of 1.6 over the entire laser aperture.

The above analysis shows that an external magnetic field is quite effective in preventing beam pinching and beam diffusion, and the magnetic fields required are modest.

To generate a guide field for our device two field coils were made. Figure 27 shows a picture of one of these. The coils were made from 36 turns of 1-1/2 inch wide by 1/16-inch thick copper strips. The coils are powered by two 100-1000 amp welding supplies supplied by AERL. Control circuitry was made so that the coils are energized 10 sec before the firing of the e-beam to allow time for the current to reach steady state and to allow time for the magnetic field to fully penetrate the laser cavity and e-gun chamber. The temperature rise due to I^2R heating in the coils during a 10 sec pulse was calculated to be negligible, so no water cooling was provided.

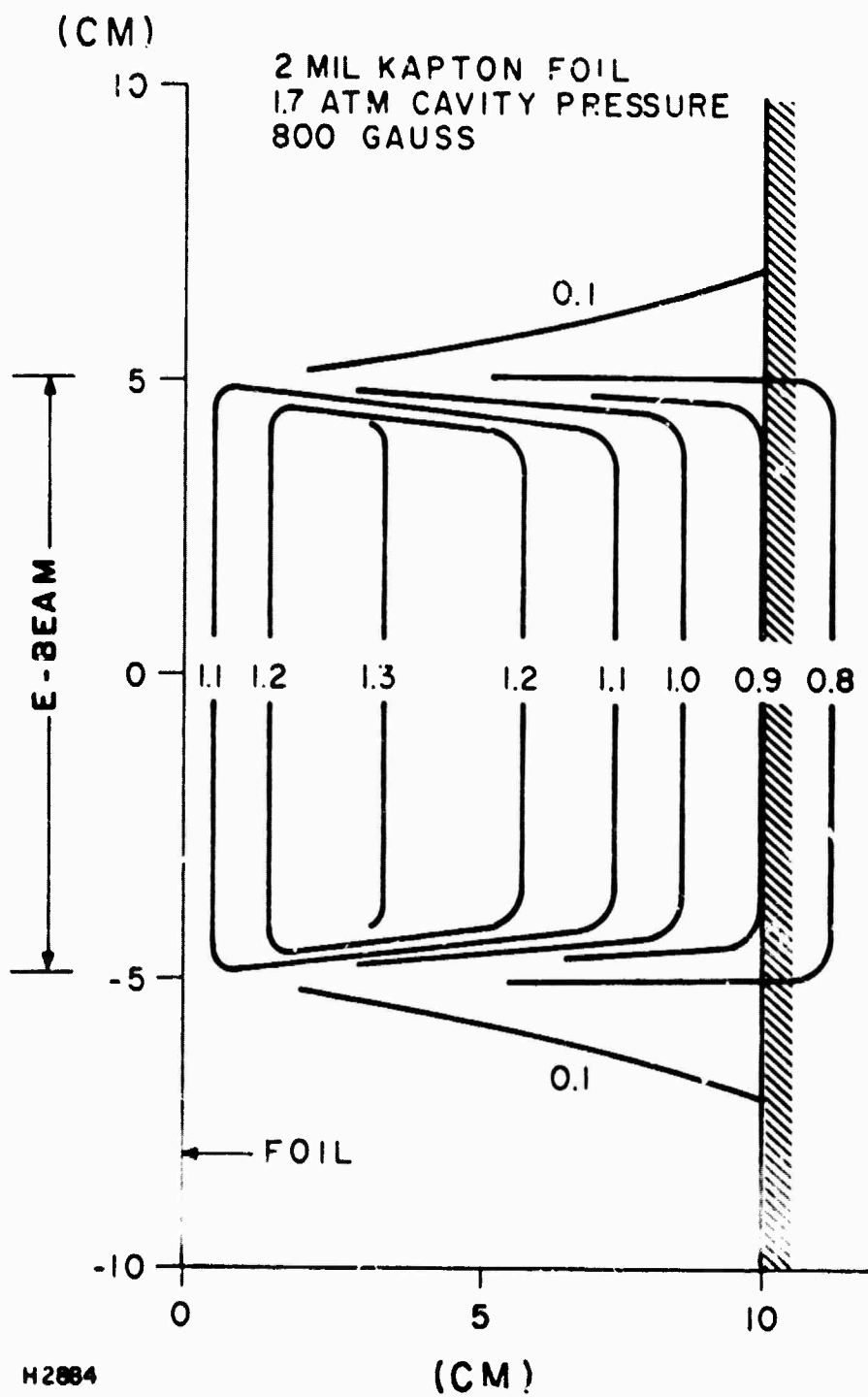
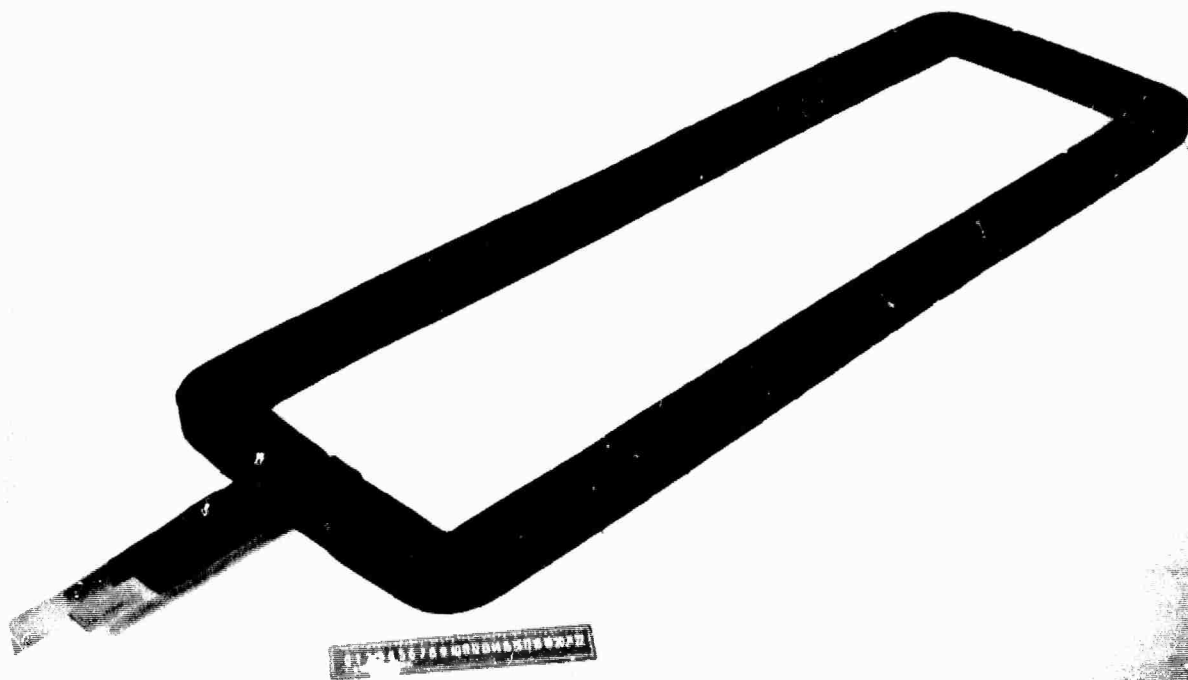


Figure 26 Calculated Contours of Constant E-Beam Energy Deposition with 800 Gauss Externally Applied Magnetic Field



G7247

Figure 27 Magnetic Field Coil

These coils were designed to fit outside the laser chamber. The location, size, and relative spacing of the coils were chosen with the aid of a computer so that the field would be uniform to within $\pm 5\%$ for the entire active laser volume and slightly divergent out to the position of the e-beam cathode. The location of the field coil is shown in Figure 28. With 580 A in each coil the field in the center of the laser region was measured to be 800 G. The measured magnetic field strength versus distance from the e-gun cathode at the midplane of the laser cavity is shown in Figure 29. The convergence in the field from the cathode to the foil is designed into the system to bring the electrons emitted by the edge blades on the cathode into the anode screen open area. These electrons, in the absence of an applied field, would impinge on the e-gun chamber faceplate outside the screen opening and be lost to the beam. The convergent B-field in this case provides the additional benefit of increasing the total transmitted current into the laser cavity.

Experimentally, the action of the guide field is shown in Figure 30. Here we compare the transmitted e-beam current, measured with the Faraday cup array, with and without an applied magnetic field. Again, the top traces are from a cup located 2.25 cm above the midplane while the bottom traces are from one at the midplane. For these measurements, a one-mil thick titanium foil was used instead of kapton to provide additional scattering to smooth out the fast spatially localized oscillations so that the large scale beam variations can be easily seen. Note that without an applied magnetic field, beam pinching is quite evident. In fact, there was almost a factor of 2 variation in the transmitted beam without a magnetic field. With the field,

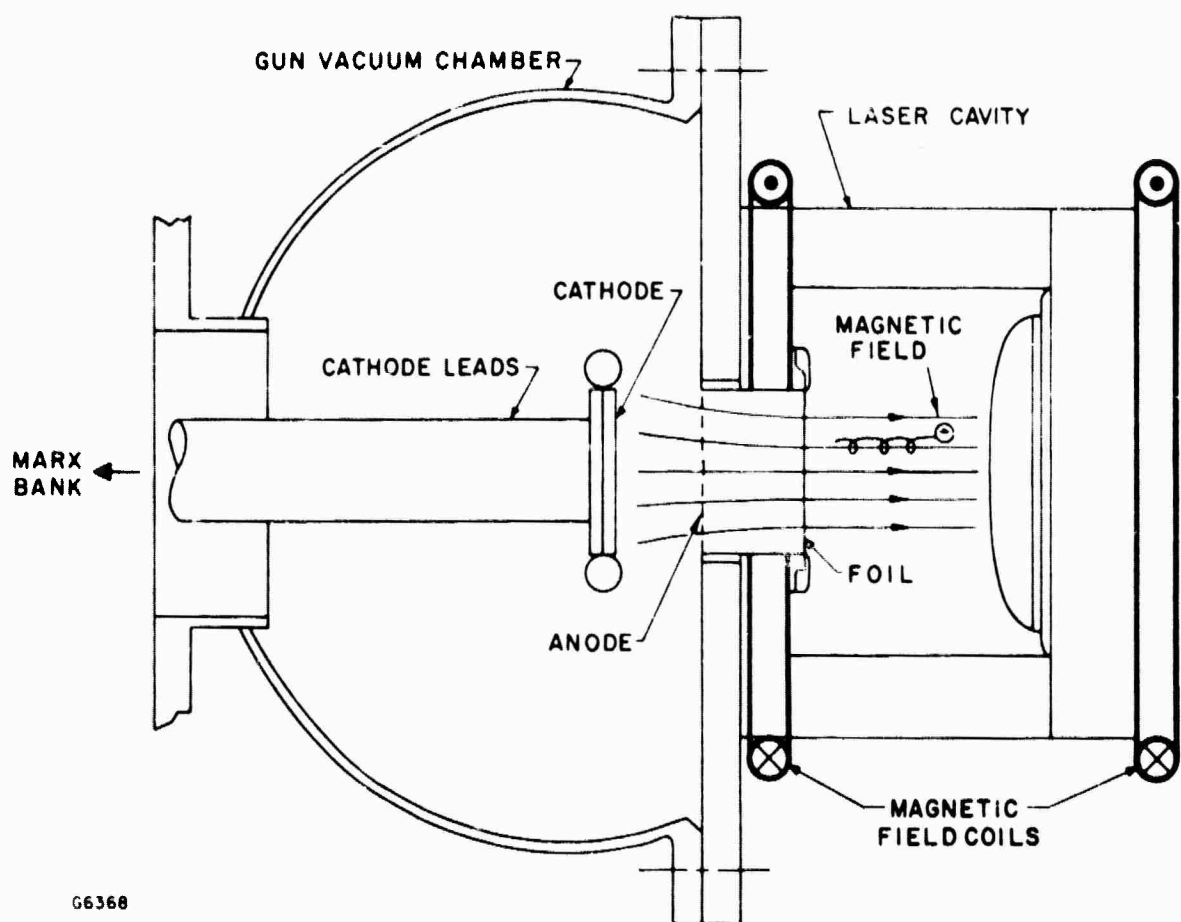
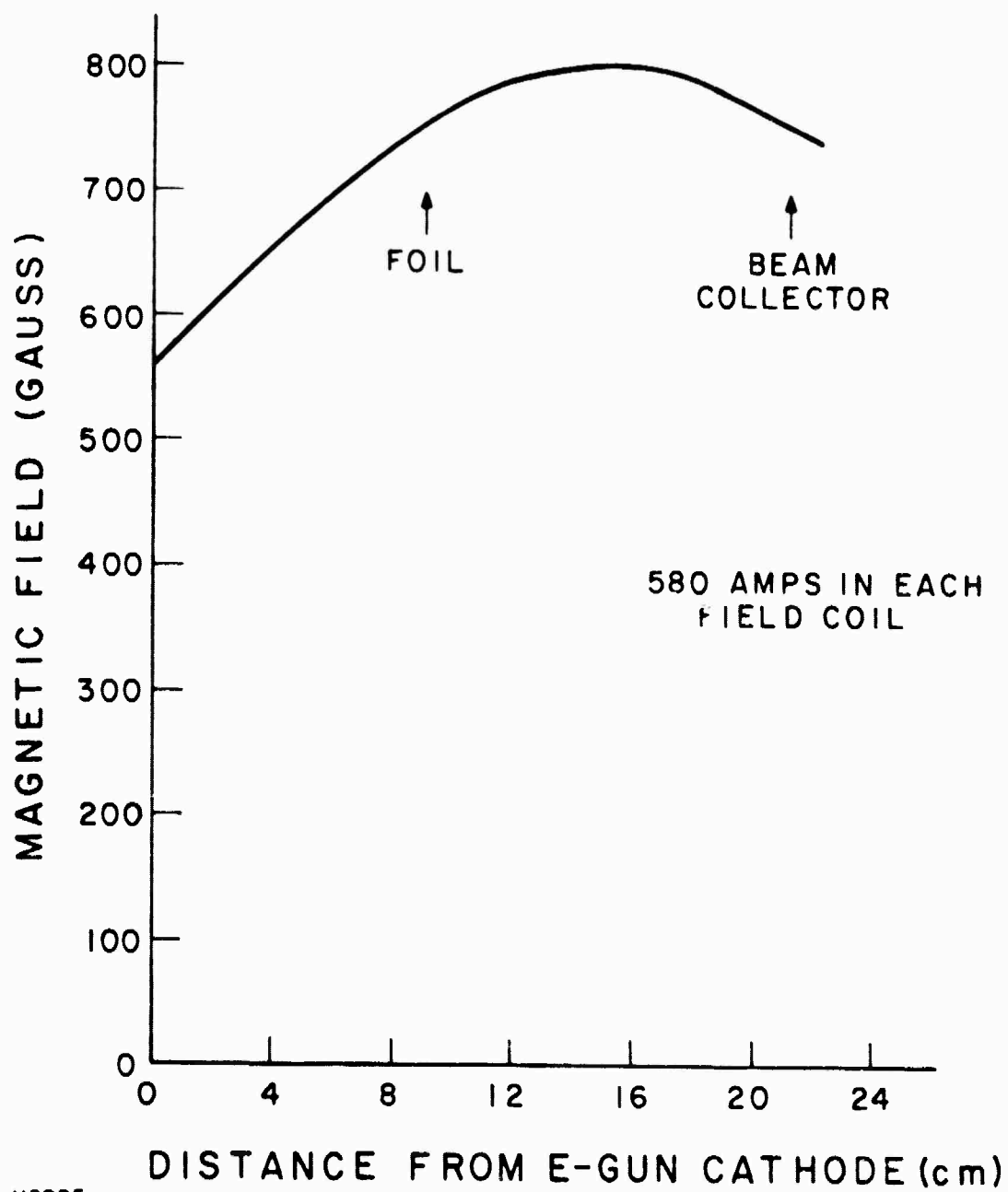


Figure 28 Cross Sections of E-Gun and Laser Cavity with Magnetic Field Coils



H2885

Figure 29 Horizontal Magnetic Field Measured Along Centerline of Device

1 MIL TITANIUM FOIL
250 kV E-BEAM

WITHOUT MAGNETIC FIELD



200 nsec/div →

800 GAUSS MAGNETIC FIELD



200 nsec/div →

TRANSMITTED E-BEAM

CURRENT $2 \text{ A/cm}^2 / \text{div}$ ↓

2.25 ABOVE BEAM

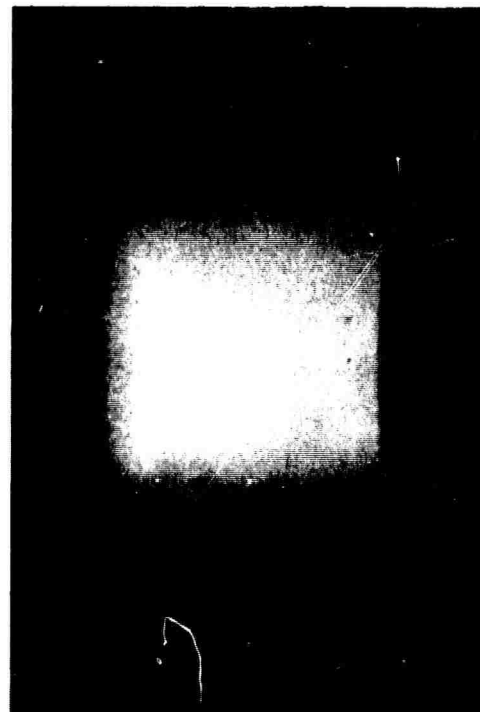
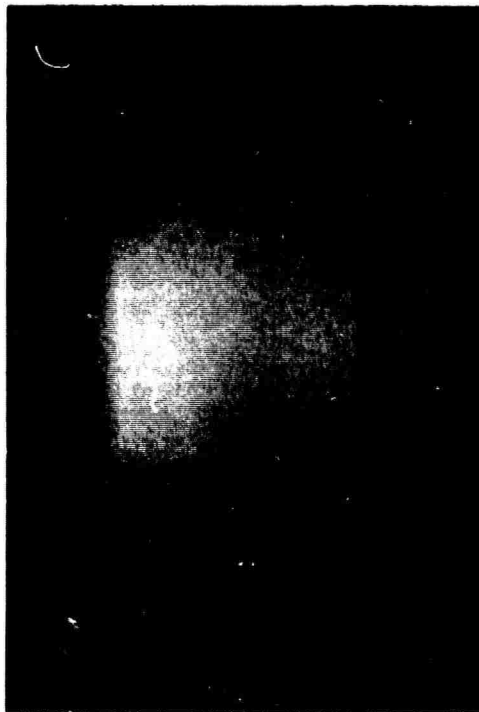
CENTER

BEAM CENTER

H2886

Figure 30 Comparison of Transmitted E-Beam Current with and without Externally Applied Magnetic Field

the beam became totally uniform. E-beam confinement in the laser cavity is clearly shown in Figure 31. Here we show two open shutter photographs, taken through one of the end windows, of the laser cavity fluorescence under e-beam excitation with and without magnetic field. Without magnetic field, scattering by the titanium foil caused the beam to spread and fill the entire cavity, while with a 800 G field, the beam was confined with negligible spreading.



NO MAGNETIC FIELD

WITH MAGNETIC FIELD (800 GAUSS)

G8047

0.2% F / 4% Kr / 95.8% Ar AT 1.5 ATM

Figure 31 Magnetic Steering of the E-Beam (1 mil Titanium Foil)

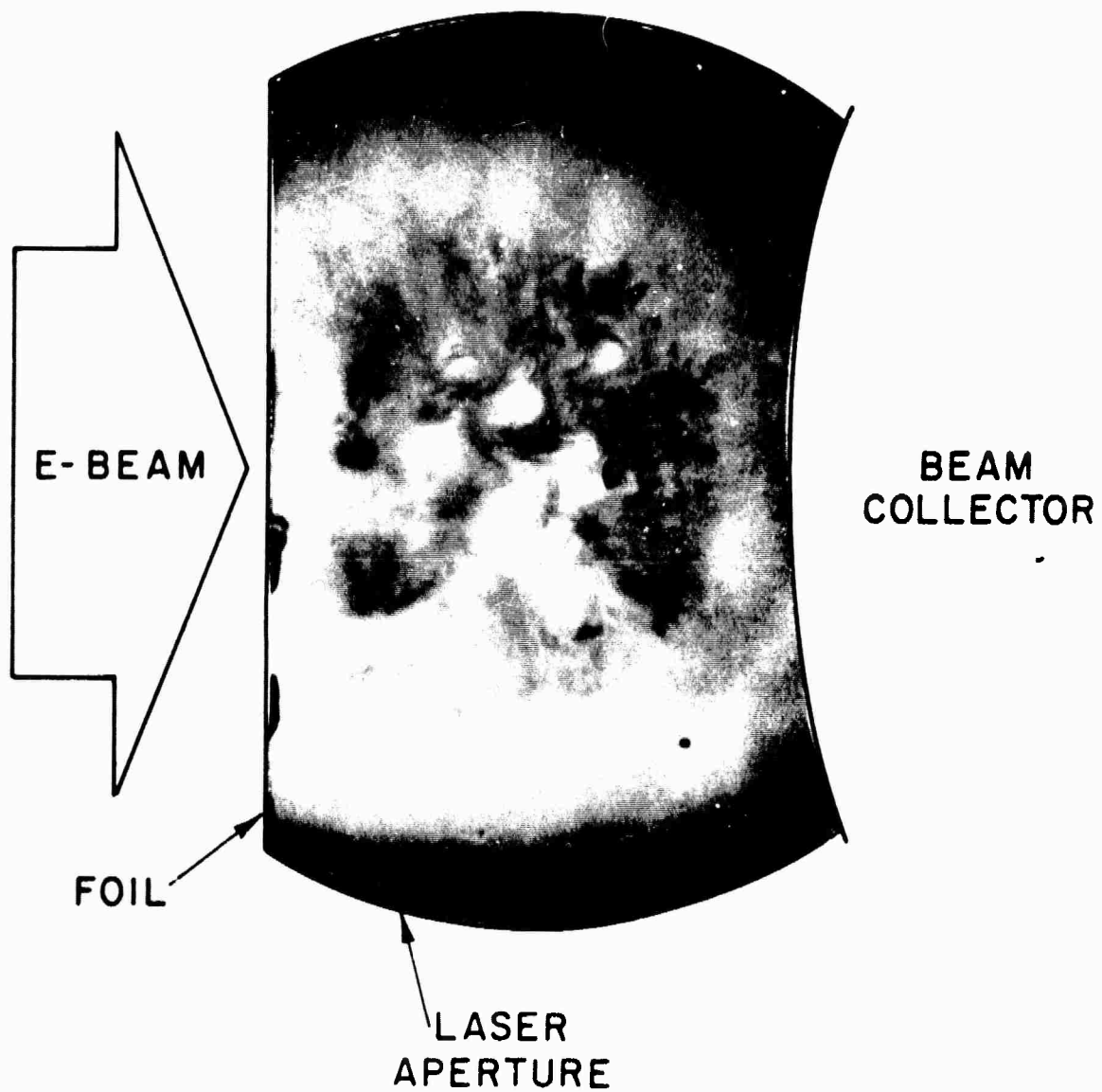
VII. E-BEAM PUMPED KrF* LASER EXPERIMENTS

With the improvement in e-beam energy deposition brought about by the application of a magnetic guide field, KrF* laser experiments were again tried. This time the results were dramatically improved. The uniformity in pumping allowed energy to be extracted efficiently over the entire 8.5 liter laser volume. Figure 32 shows a typical laser output burn pattern. Note that the laser fell off somewhat at the outer edges near the beam collector which was due to the residual beam diffusion over one Larmor radius (≈ 1 cm) as theoretically predicted in Figure 25.

The e-gun cathode voltage and current traces are shown in Figure 33. A small portion of the output laser beam was scattered into a filtered photodiode (S-5) by placing a wire in the beam. The transmission of the filter was peaked at 2485 \AA with FWHM of 25 \AA . A typical laser pulse shape is also displayed in Figure 33.

The laser output energy was monitored by a Scientek Model 364 calorimeter with an 8-inch diameter head. Nextel flat black paint was used on the heat-sensitive surface. The calorimeter was calibrated absolutely by using the resistive heater embedded behind the heat sensitive surface and a precision voltage source. Considerable vaporization of the painted surface occurred during every shot of the laser. No attempt was made to correct our energy measurements for imperfect absorption by the calorimeter surface nor for energy lost due to paint vaporization. Therefore, our measurements were probably somewhat low. In any case, the results reported here can be taken as a conservative measure of what was actually coming out of the laser.

KrF* LASER BURN PATTERN
(800 G MAGNETIC FIELD)

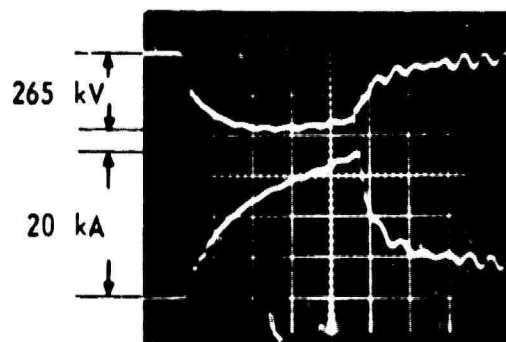


DIRECT ELECTRON BEAM PUMPING

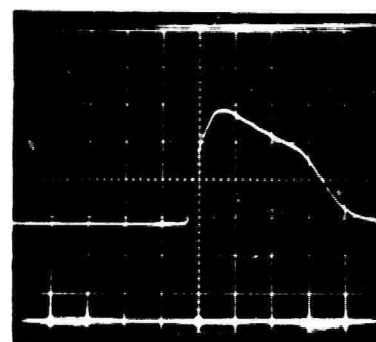
H2882

Figure 32 Laser Output Burn Pattern

CATHODE VOLTAGE



LASER PULSE



G7758

200 nsec div

Figure 33 E-Beam and Laser Characteristics

Major results of these experiments are given in Table 3. Also shown for comparison are calculated predictions of our kinetics-comprehensive KrF* laser code. Similar agreement has been achieved over a wide range of laser operating conditions. The agreement of the laser code with the experimental large scale laser results increases confidence in code predictions for larger scale devices.

TABLE 3
COMPARISON OF MODEL PREDICTIONS WITH EXPERIMENT

0.2% F₂/4% Kr/95.8% Ar @ 1.7 atm

250 kV, 11.5 A/cm² E-Beam

600 nsec Pulse Length

70% Output Coupling

	<u>Predictions</u>	<u>Measurements</u>
Laser Energy/Energy Deposited	9.8%	9%
Energy Extraction	12.6 J/1	12 J/1
Extraction Efficiency	46%	

REFERENCES

1. Mangano, J. A. and Jacob, J. H. , Phys. Lett. 27, 495 (1975).
2. Jacob, J. H. , J. Appl. Phys. 45, 467 (1974).
3. Brau, C. A. and Ewing, J. J. , private communication.
4. Krauss, M. , NBS, private communication.
5. Peterson, L. R. and Allen, J. E. , J. Chem. Phys. 56, 6068 (1972).
6. Flannery, M. R. , in Case Studies in Atomic Collision Physics 2, edited by McDaniel, E. W. and McDowell, M. R. C. , North Holland, Amsterdam, 1972, p. 3.
7. Michels, H. , United Technologies, private communication.
8. Ewing, J. J. , LLL, private communication.
9. McDaniel, E. W. , Cermak, V. , Dalgarno, A. , Ferguson, E. E. and Friedman, L. , Ion-Molecule Reactions (Wiley-Interscience, New York, 1970) p. 338.
10. Bohme, D. K. , Adams, N. G. , Moselman, M. , Dunkin, D. B. and Ferguson, E. E. , J. Chem. Phys. 52, 5094 (1970).
11. For a detailed discussion of this verification procedure see Rokni, M. , Jacob, J. H. , Mangano, J. A. and Brochu, R. , to appear in Appl. Phys. Lett. , May (1977).
12. Dunning, T. H. and Hay, P. J. , Appl. Phys. Lett. 28, 649 (1976).
13. Rokni, M. , Jacob, J. H. and Mangano, J. A. (unpublished).
14. We have recently measured the exchange reaction by observing the decrease in the ArF^{+} fluorescence and obtained a value of $k_e \approx 6.5 \times 10^{-18} \text{ cm}^3/\text{sec}$. This work was reported by us at the 7th Winter Colloquium on High Power Visible Lasers, Park City, Utah, Feb. 16 - 18 (1977).
15. The steady state assumption is valid because the dominant rates are much less than the 300 ns e-beam pulse.
16. Hawryluk, A. , Mangano, J. A. and Jacob, J. H. , Proceedings of the Third Summer Colloquium on Electronic Transition Lasers, Snowmass, 1976 (unpublished).

17. Tellinghuisen, J., Hays, A.K., Hoffman, J.M. and Tiscione, G.C., J. Chem. Phys. 65, 4473 (1975).
18. Steunenberg, R. and Vogel, R., J. Am. Chem. Soc. 78, 901 (1956).
19. Ma ¹¹, A., Phys. Rev. A 3, 251 (1971).
20. Hyman, H., (AERL) private communication.
21. Stevens, W., Gardner, M. and Karo, A., (unpublished).
22. Krauss, M., private communication.

APPENDIX A

FAST BEAM CURRENT DENSITY FLUCTUATION

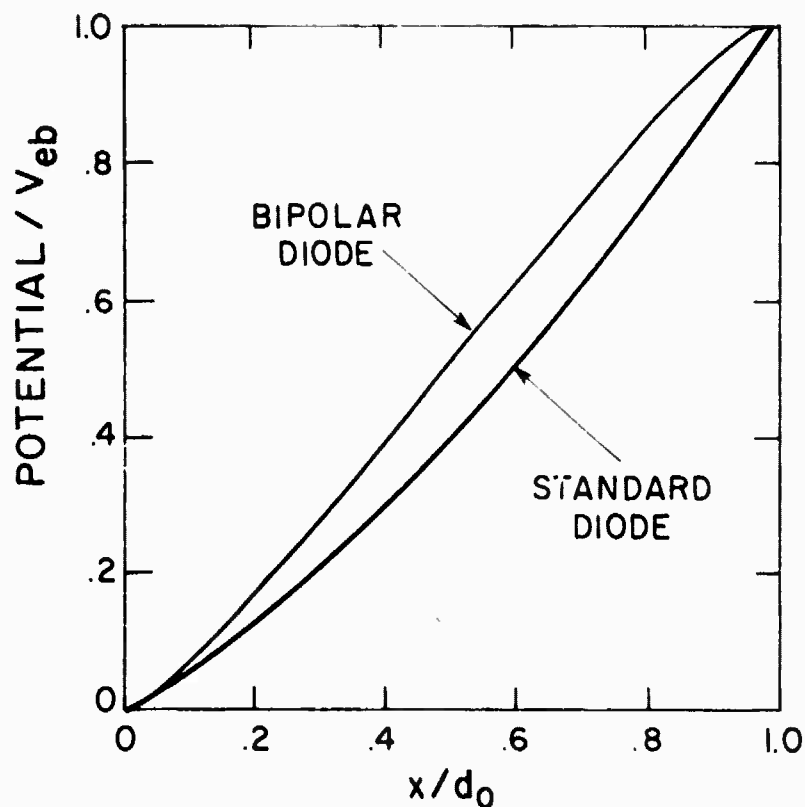
In addition to the spatial inhomogeneity in e-beam current density caused by beam pinching, a faster temporal beam fluctuation, with 2 to 1 variations in beam current density averaged over a beam area of 1 cm^2 , is observed. Typically, the amplitude of the fluctuation becomes large ~ 200 to 300 nsec into the pulse. The instability is characterized by increases in beam current density by a factor of 2 in a time which can be as short as 25 nsec . We have found that there is no apparent temporal correlation in these fluctuations in the beam current density between 1 cm^2 samples taken 2 cm apart. In addition, there is essentially no shot to shot correlation between beam samples taken at the same transverse position.

These fluctuations can be caused by positive ions which are created at the gun anode. The ions can be generated when the surface of the solid anode sections is heated by the e-beam. In $200 - 300 \text{ nsec}$, these parts are heated by $\sim 100^\circ\text{C}$ so that some of the surface contaminants are vaporized and absorbed gases are desorbed. The e-beam and local electric fields can then ionize the evolved gases and produce positive ions. These ions are then accelerated by the diode field and can partially neutralize the electron space charge. A new quasi-equilibrium results in which both the electron and ion current densities are space-charge-limited. Langmuir⁽¹⁾

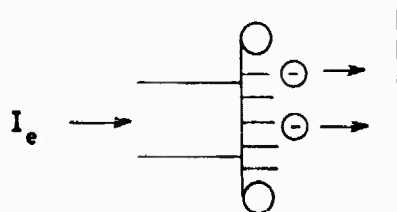
(1) Langmuir, L., Phys. Rev. 33, 954 (1929).

has shown that for a planar "bipolar diode", the space-charge-limited electron current density can reach 1.86 times that obtained with no positive ions. The potential across the diode gap is plotted in Figure A-1 for both electron space-charge-limited conditions and for the bipolar diode case.

In the case where a planar plasma electron source is present at the cathode but where only small patches of ions are generated at the anode, an even larger change in the electron current density is possible. Spatially localized potential perturbations can lead to beam focusing. This effect is illustrated graphically by Figure A-2. The fastest time scale on which the local beam current density can increase is just the transit time of these ions across the anode-cathode gap. Assuming a typical anode-cathode spacing of 7 cm and a cathode potential of -300 kV, the transit time for a H^+ ion across this gap when accelerated by the space-charge-modified electric field is 28 nsec. If the electron space charge were completely neutralized by the positive ions, the ion transit time would be ~19 sec. Therefore, the ion transit time across the diode gap is found to be consistent with the shortest observed beam current growth time of ~25 nsec. The local reestablishment of the original diode conditions then depends upon the time history of ion creation at the anode and the density of the plasma. Positive ions can be created randomly at the gun anode by desorption and vaporization followed by beam and electric field ionization. However, at the gun anode, the plasma formation time is longer (heating time by beam) and the plasma is likely to be spatially nonuniform across the anode surface. Again, this hypothesis is consistent with the experimental fact that the large beam current fluctuations develop 200 to 300 nsec into the beam pulse and have small spatial correlation lengths.

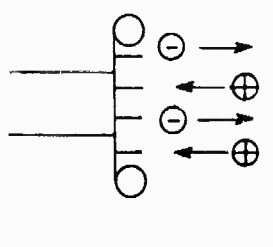


● ELECTRON EMISSION FROM CATHODE ONLY



$$I_{e \text{ BIPOLAR}} = 1.86 I_e$$

● BIPOLAR EMISSION



G7208

Figure A-1 Potentials for both Unipolar and Bipolar Diodes are Shown. In the planar case the electron current density in the bipolar case is 1.86 times the electron current density in the unipolar case.

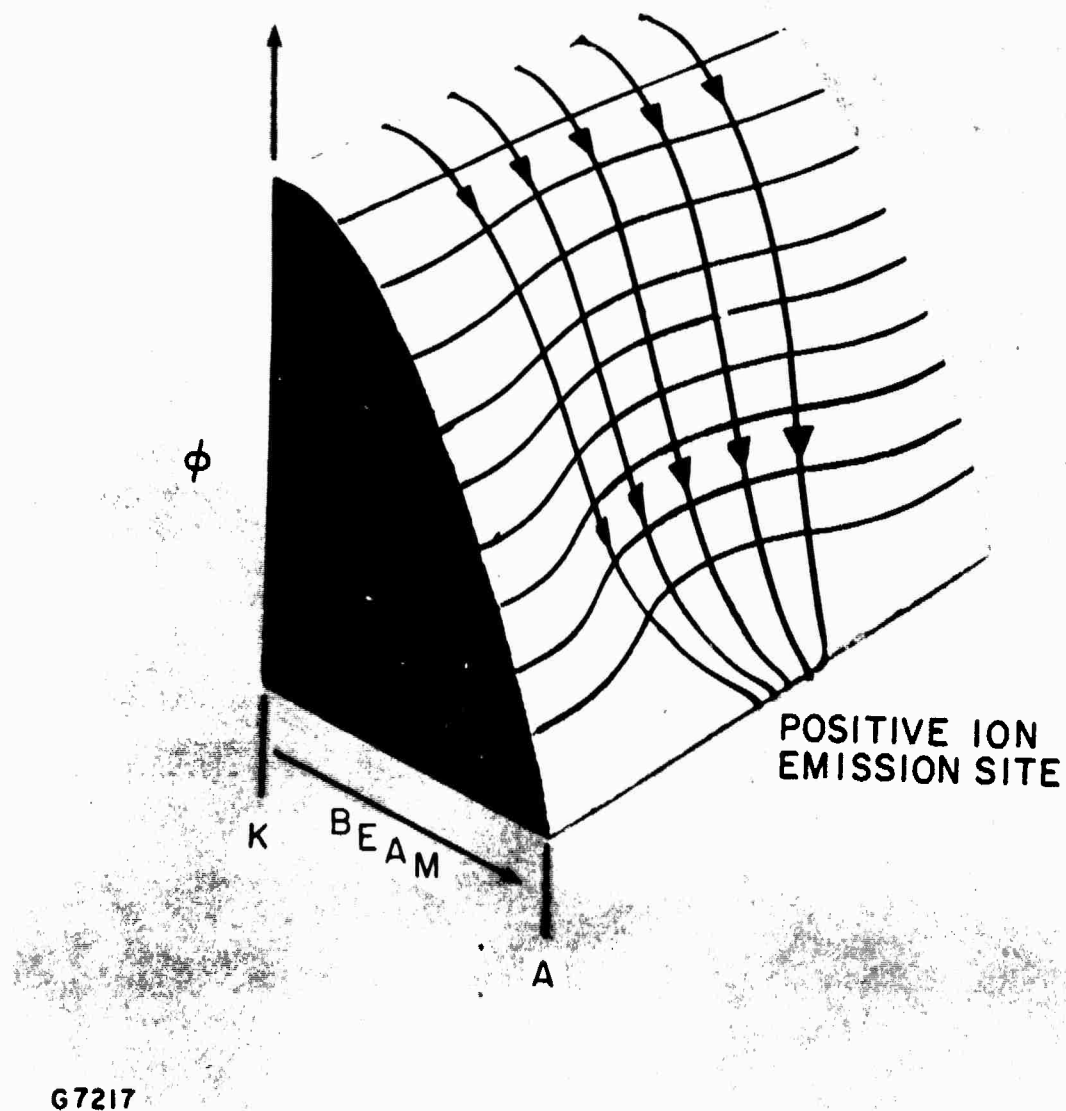


Figure A-2 Equipotential Contours for the Case of Local Anode Ion Sources

Additional evidence of the bipolar diode effect is seen in Figure A-3. Here we compare e-gun cathode voltage and current for two shots taken under identical conditions, but with two different anode screen materials. The top traces were taken with a stainless steel anode screen while the bottom traces were taken with a tungsten anode screen. Since tungsten has a higher Z , compared with S. S. , surface heating by the e-beam is expected to be much more severe. This will lead to higher ion formation at the anode and correspondingly higher effective diode closure velocity. This is indeed what we observe.

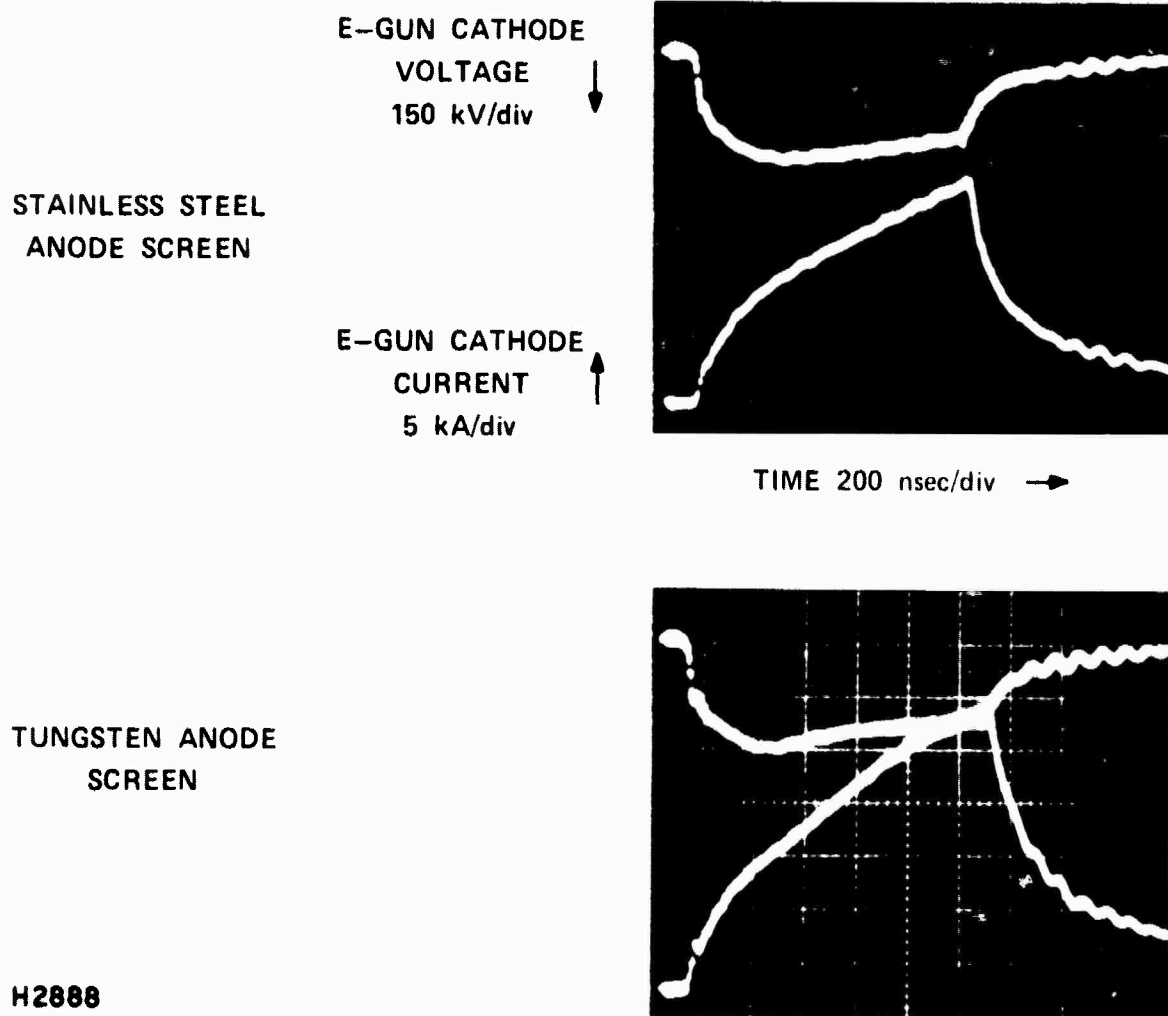


Figure A-3 E-gun Cathode Voltage and Current with SS and Tungstun Anode Screens

APPENDIX B

HIGH ENERGY ELECTRON SCATTERING

Electron transport through a single slab has previously been treated in great detail,⁽¹⁾ so we will only briefly outline the theory. For a beam of electrons uniform in the x and y directions, striking a plane parallel plate that has a thickness t in the z-direction, the Boltzmann equation can be written as

$$\mu \frac{\partial f}{\partial z} = N \int [f(z, \underline{u}') - f(z, \underline{u})] \sigma(\mu_0) d\underline{u}' \quad (\text{B-1})$$

where μ is the cosine of the angle between the electron trajectory and the z axis, μ_0 is the cosine of the angle between the incident and scattered electron trajectories and \underline{u} is the unit vector in the direction of the electron motion.

Expanding the distribution function and the scattering cross section as a sum of Legendre polynomials:

$$f = \sum_{\ell} A_{\ell} P_{\ell}(\mu) \quad (\text{B-2})$$

and

$$\sigma = \sum_{\ell} \sigma_{\ell} P_{\ell}(\mu_0) \quad (\text{B-3})$$

Substituting expansions (B-2) and (B-3) into Eq. (B-1) and making use of both the orthogonality relation and addition theorem for Legendre polynomials, Eq. (B-1) becomes

(1) Jacob, J.H., Phys. Rev. A8, 226 (1973).

$$\left(\frac{\ell}{2\ell-1}\right) \frac{\partial A_{\ell-1}}{\partial z} + \frac{(\ell+1)}{(2\ell+3)} \frac{\partial A_{\ell+1}}{\partial z} + 2\pi N A_{\ell} \int_{-1}^{+1} d\mu \sigma(\mu) [1 - P_{\ell}(\mu)] = 0 \quad (B-4)$$

The scattering cross section is, of course, the screened Rutherford that is modified to include relativistic effects and inelastic scattering by orbital electrons. Relativistic effects for small Z , i.e., $Z < 27$, can be included by use of the McKinley-Feshbach expansion of the complete Mott formulas. Assuming the Thomas-Fermi atomic model, the screening angle η is given by

$$\eta = \frac{1}{4} \left[\frac{\hbar}{p} \frac{1.12Z^{1/3}}{0.885 a_0} \right]^2$$

where p is the momentum of the electron and a_0 the Bohr radius. Making the following substitutions

$$G_{\ell} = 2\pi N \int_{-1}^{+1} d\mu \sigma(\mu) (1 - P_{\ell}(\mu))$$

$$\frac{1}{\lambda} = \frac{G_1}{2} = \frac{\pi N Z (Z+1)}{p^2 v^2} e^4 \left\{ \ln(1 + 1/\eta) - \frac{1}{1+\eta} + 2\pi\alpha\beta - (\beta^2 + \pi\beta b) \right\} \quad (B-5)$$

where λ is the transport mean free path, $\zeta = z/\lambda$ and $\alpha = Z/137$. Equation (B-4) can then be rewritten as

$$\left(\frac{\ell}{2\ell-1}\right) \frac{\partial A_{\ell-1}}{\partial \zeta} + \frac{(\ell+1)}{(2\ell+3)} \frac{\partial A_{\ell+1}}{\partial \zeta} + \frac{2G_{\ell}}{G_1} A_{\ell} = 0 \quad (B-6)$$

Equation (B-6) forms an infinite set of coupled differential equations with constant coefficients. To obtain a solution for the scattering through a slab the boundary conditions at each surface have to be included. Consider an e-beam of arbitrary but known distribution function impinging on a target thickness t . Hence at $\zeta = 0$, $f(\mu \geq 0, \zeta = 0)$ is known and at the far boundary

$\zeta = t/\lambda$ there are no particles entering the target, hence $f(\mu \leq 0, \zeta = t/\lambda) = 0$.

The above boundary conditions can be written as

$$\left. \begin{aligned} f(\mu \geq 0, \zeta = 0) &= \sum_{n=0}^{\infty} b_{2n+1} P_{2n+1}(\mu) \\ \text{and} \\ f(\mu \leq 0, \zeta = t/\lambda) &= \sum_{n=0}^{\infty} c_{2n+1} P_{2n+1}(\mu) = 0 \end{aligned} \right\} \quad (\text{B-7})$$

In Eq. (B-7) use has been made of the fact that the odd Legendre polynomials form a complete set in the half space. This choice is by no means unique; one could, for example have chosen the even polynomials. However, as the current is a more readily measurable quantity than density, odd polynomials are used. Thus there is an infinite set of boundary conditions at each surface, but because of the truncation there are only $N + 1$ unknowns. Hence, we specify $(N + 1)/2$ conditions at each boundary. Making use of orthogonality, one has Marshak's boundary condition

$$\left. \begin{aligned} \int_0^1 d\mu P_{2n+1} f(\mu, \zeta = 0) &= \frac{b_{2n+1}}{4n+3} \\ \text{and} \\ \int_{-1}^0 d\mu P_{2n+1} f(\mu, \zeta = t/\lambda) &= 0 \end{aligned} \right\} \quad n = 0 \dots \frac{N}{2} \quad (\text{B-8})$$

The above analysis assumes that the electron energy is strictly a constant. This is clearly not the case. We can allow for energy variation by dividing the slab into many layers and allowing the electron energy to vary from one layer to the next. At the free surfaces the boundary conditions are given by Eq. (B-8), while at the interface $Z = Z_1$, we assume

that there is no discontinuity in the distribution function as one goes from one layer to the next. This continuity can be insured by setting

$$A_{\ell 1}(Z_1) = A_{\ell 2}(Z_1) \quad \ell = 1, 2, \dots, N$$

where $A_{\ell 1}$ and $A_{\ell 2}$ are the coefficients of the ℓ^{th} Legendre polynomial in the two layers.

Energy loss is included assuming that the electron continuously loses energy as it penetrates the material. The effects of straggling are neglected. The path length of most of the electrons will be greater than the thickness of the target considered because of elastic scattering. To a first approximation it is assumed that only elastic scattering exists. The resulting angular spread of the electrons can be computed and hence the average electron trajectory. The target is divided into a number of thin layers and in each layer we assume that the energy loss is given by

$$\Delta w = \frac{dw}{dS} \langle S \rangle \quad (\text{B-9})$$

where w is the electron energy and dw/dS is the Bethe stopping power given by

$$\frac{dw}{dS} = \frac{2\pi e^4}{mc^2\beta^2} \frac{N_a \rho}{A} Z \ln \left[\frac{T^2(T+2)}{2(I/mc^2)^2} + 1 - \beta^2 + T^2/8 - (2T+1)\ln 2/(T+1)^2 \right] \quad (\text{B-10})$$

where N_a is Avogadro's number, A the atomic weight, T the kinetic energy of the electron in units of the electron rest energy and I is the mean excitation energy. ⁽²⁾ For 1 we have used the values recommended by Berger.

$\langle S \rangle$ is the average path length of the electron in the given slab and it is given by

(2) Berger, M. J. and Seltzer, S. M., NAS-NRC Publication No. 1133 (unpublished) (1964).

$$\langle S \rangle \approx \frac{t}{\langle \cos \theta \rangle} \quad (\text{B-11})$$

where t is the slab thickness and $\langle \cos \theta \rangle = 1/2 (\langle \cos \theta \rangle_1 + \langle \cos \theta \rangle_2)$, $\langle \cos \theta \rangle_1$ and $\langle \cos \theta \rangle_2$ being the average value of μ at the beginning and end of each slab for the particles traveling in the positive μ direction only. This ignores the backscattered particles (in computing the average path length only). The error so introduced is expected to be small, however, if the thickness of each layer is much less than λ , the transport mean free path. The multi-layer theory also neglects the absorption of electrons. Because of these approximations it has been found convenient to connect the multilayer theory to the age diffusion theory. The age theory is just the P_1 approximation with the inclusion of energy loss. We have extended the age theory to include effects of an applied electric field. ^(3, 4)

(3) Jacob, J. H., J. App. Phys. 467 (1964).

(4) Jacob, J. H. and Bethe, H. A., (unpublished).